Relation between Baroclinity, Horizontal Vorticity, and Mesocyclone Evolution in the 6–7 April 2018 Monroe, Louisiana, Tornadic Supercell during VORTEX-SE

MICHAEL J. HOSEK,[a,b] CONRAD L. ZIEGLER,[b,a] MICHAEL I. BIGGERSTAFF,[a] TODD A. MURPHY,[c] AND ZHIEN WANG[d]

[a] *School of Meteorology, University of Oklahoma, Norman, Oklahoma*
[b] *NOAA/National Severe Storms Laboratory, Norman, Oklahoma*
[c] *University of Louisiana–Monroe, Monroe, Louisiana*
[d] *University of Colorado Boulder, Boulder, Colorado*

(Manuscript received 7 November 2022, in final form 23 August 2023, accepted 28 August 2023)

ABSTRACT: This case study analyzes a tornadic supercell observed in northeast Louisiana as part of the Verification of the Origins of Rotation in Tornadoes Experiment Southeast (VORTEX-SE) on 6–7 April 2018. One mobile research radar (SR1-P), one WSR-88D equivalent (KULM), and two airborne radars (TAFT and TFOR) have sampled the storm at close proximity for ~70 min through its mature phase, tornadogenesis at 2340 UTC, and dissipation and subsequent ingestion into a developing MCS segment. The 4D wind field and reflectivity from up to four Doppler analyses, combined with 4D diabatic Lagrangian analysis (DLA) retrievals, has enabled kinematic and thermodynamic analysis of storm-scale boundaries leading up to, during, and after the dissipation of the NWS-surveyed EF0 tornado. The kinematic and thermodynamic analyses reveal a transient current of low-level streamwise vorticity leading into the low-level supercell updraft, appearing similar to the streamwise vorticity current (SVC) that has been identified in supercell simulations and previously observed only kinematically. Vorticity dynamical calculations demonstrate that both baroclinity and horizontal stretching play significant roles in the generation and amplification of streamwise vorticity associated with this SVC. While the SVC does not directly feed streamwise vorticity to the tornado–cyclone, its development coincides with tornadogenesis and an intensification of the supercell's main low-level updraft, although a causal relationship is unclear. Although the mesoscale environment is not high-shear/low-CAPE (HSLC), the updraft of the analyzed supercell shares some similarities to past observations and simulations of HSLC storms in the Southeast United States, most notably a pulse-like updraft that is maximized in the low- to midlevels of the storm.

SIGNIFICANCE STATEMENT: The purpose of this study is to analyze the airflow and thermodynamics of a highly observed tornado-producing supercell. While computer simulations can provide us with highly detailed looks at the complicated evolution of supercells, it is rare, due to the difficulty of data collection, to collect enough data to perform a highly detailed analysis on a particular supercell, especially in the Southeast United States. We identified a "current" of vorticity—rotating wind—that develops at the intersection of the supercell's rain-cooled outflow and warm inflow, similar to previous simulations. This vorticity current develops and feeds the storm's updraft as its tornado develops and the storm intensifies, although it does not directly enter the tornado.

KEYWORDS: Updrafts/downdrafts; Mesocyclones; Supercells; Vorticity; Cold pools; Convective-scale processes

1. Introduction

High-resolution observational analyses of tornadic supercells in the Southeast United States are rare compared to studies from the Great Plains. Study in this region is particularly important due to the overlap of environmental and socioeconomic factors resulting in the Southeast region having the greatest concentration of tornado-related fatalities (Ashley 2007). Southeast tornado events tend to occur in environments with lower convective available potential energy (CAPE) and larger vertical wind shear than their Great Plains counterparts, making them more difficult to accurately forecast and warn on (Anderson-Frey et al. 2019) and changing some of the fundamental storm-scale structures we traditionally associate with supercells in the Great Plains (Wade and Parker 2021, hereafter WP21). Studying the structure of storm-scale features and how they influence the supercell's mesocyclone is critical for our ability to forecast and understand the complex physical processes in the low levels of supercells, including tornadogenesis.

Decades of studies have shown that the midlevel mesocyclone [defined here as 2–5 km AGL following Skinner et al. (2014); all heights are above ground level unless noted otherwise] develops from the tilting and stretching of ambient horizontal vorticity as air parcels are carried into the updraft (Barnes 1970; Rotunno 1981; Davies-Jones 1984; Lilly 1986; Adlerman et al. 1999; Mashiko 2016). Although this process is insufficient to develop a near-surface mesocyclone—tilting occurs as the updraft is carrying air parcels up away from the surface (Davies-Jones 1982)—it may still serve as a significant source of vorticity for the low-level (0.25–1 km) mesocyclone (e.g., Coffer et al. 2023). The generation of near-surface (below 250 m) rotation has been attributed to friction effects, although this is a field of active investigation (e.g., Schenkman et al. 2014; Yokota et al. 2018; Roberts et al. 2020; Tao and Tamura 2020; Fischer and Dahl 2022). However, other observational and simulation studies have postulated that the tilting

Corresponding author: Michael J. Hosek, hosek.michael@ou.edu

DOI: 10.1175/MWR-D-22-0313.1

of horizontal vorticity generated baroclinically along storm-scale boundaries may also contribute to the development of a low-level mesocyclone and near-surface rotation (e.g., Davies-Jones and Brooks 1993; Rotunno and Klemp 1985; Wicker and Wilhelmson 1995; Markowski et al. 2012b; Dahl et al. 2014; Parker and Dahl 2015; Dahl 2015; Marquis et al. 2016; Fischer and Dahl 2022). The baroclinic mechanism (also known as the solenoidal mechanism) generates horizontal vorticity via a secondary circulation induced by the density difference across a thermodynamic boundary, with warm air rising while moving toward the cool air and cool air sinking while moving toward the warm air (Davies-Jones 2000).

High-resolution supercell simulations have depicted a concentrated flow of streamwise vorticity—the "streamwise vorticity current" (SVC)—extending along a forward-flank baroclinic boundary at low levels and feeding the low-level mesocyclone (Orf et al. 2017; Schueth et al. 2021, hereafter S21; Finley et al. 2023). While many previous simulations identified regions of enhanced baroclinically generated streamwise vorticity entering the low-level mesocyclone (e.g., Klemp and Rotunno 1983; Rotunno and Klemp 1985; Wicker and Wilhelmson 1995; Adlerman et al. 1999; Beck and Weiss 2013, hereafter BW13; Tanamachi et al. 2013), the Orf et al. (2017) simulation was the first to spatially resolve it as a coherent horizontal vortex. A simulated SVC typically develops as a combination of 1) baroclinically generated streamwise vorticity in a Kelvin–Helmholtz wave-like circulation at the baroclinic boundary and 2) horizontal stretching of both ambient and baroclinically generated streamwise vorticity as airflow accelerates toward the low-level updraft (S21). Due to the SVC's narrow width and confinement within the lowest ~1 km, obtaining even just single-radar data with the necessary spatial resolution is challenging, much less multiradar analyses. Independent low-level in situ thermodynamic observations are also rare due to the hazards of flying or releasing instruments into these portions of supercells, although there has been recent progress with the deployment of swarms of balloon-borne sondes (e.g., Markowski et al. 2018; Diedrichsen et al. 2020; Bartos et al. 2022).

Numerous low-level boundaries have been identified in the supercell forward-flank downdraft (FFD) as the result of diabatic cooling from rain evaporation and graupel/hail melting (Fig. 1, from BW13). The BW13 simulation provided evidence that, in addition to the rear-flank gust front (RFGF), there are two kinematic–thermodynamic boundaries: the left-flank convergence boundary (LFCB) and the forward-flank convergence boundary (FFCB). Unlike the RFGF, which features a wind shift and strong, gusty winds, the LFCB and FFCB feature subtle confluence within a long fetch of flow extending from the forward flank to the low-level updraft, with the LFCB featuring a stronger equivalent potential temperature gradient (BW13; S21). The FFCB in a typical supercell extends into the inflow and across the forward anvil precipitation region, separating unmodified inflow air from air which has been slightly diabatically cooled in the distant forward flank. Both of these forward-flank boundaries in simulations have produced baroclinically generated streamwise horizontal vorticity, with some studies placing the SVC along the FFCB (BW13; S21).

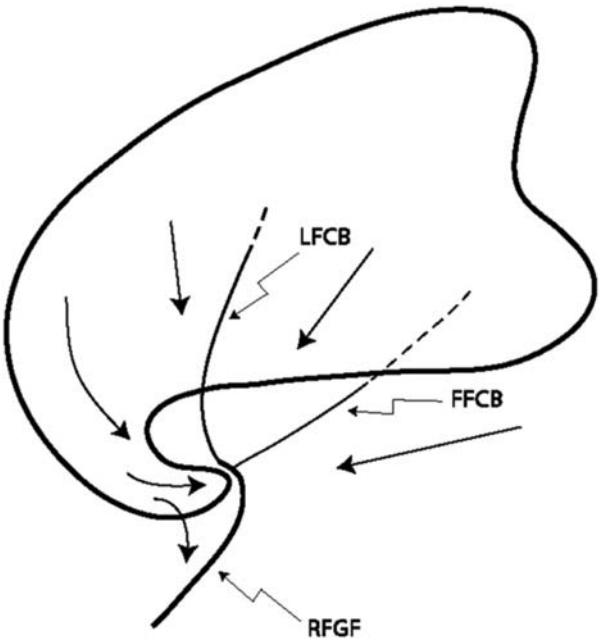

FIG. 1. The conceptual model of a typical steady-state supercell, featuring the surface-based FFCB, LFCB, and RFGF boundary locations (black solid = formed boundary; black dashed = diffuse or forming boundary), storm-relative streamlines, and black-outlined reflectivity (BW13).

There is a dearth of literature on supercells in the Southeast region, both observed and modeled, due to the difficulty in obtaining storm observations and the decades-long focus on Great Plains convection. High-shear/low-CAPE (HSLC) environments—environments with less than 1000 J Kg^{-1} MLCAPE and greater than 18 m s^{-1} 0–6-km shear (WP21)—are common in the Southeast, and the majority of EF1+ tornadoes in HSLC environments occurs there (Sherburn et al. 2016). Murphy and Knupp (2013) used a synthetic dual-Doppler technique to study two supercells which passed near a WSR-88D site in Tennessee and showed that supercell updrafts in HSLC environments maximize below 4 km, not near the storm top as in typical Great Plains supercells. Knupp et al. (2014) reported dual-Doppler analyses from the 27 April 2011 tornado outbreak, the first analysis documenting a mesoscale convective vortex (MCV) within a northern Alabama quasi-linear convective system (QLCS) and the second analysis probing the Cullman, Alabama, supercell which produced a violent tornado. These results have been reproduced in some of the few modeling studies of HSLC supercells, which demonstrate the importance of dynamic perturbation pressure forces in HSLC updrafts (Sherburn and Parker 2019; WP21). In a supercell, the low-level updraft is driven primarily by upward-directed perturbation pressure forces resulting from large low- and midlevel mesocyclonic vertical vorticity ζ by the approximate inverse relationship between perturbation pressure and enstrophy in pure rotation of the form $\pi' \sim -\zeta^2$, where π is the Exner function (Klemp and Rotunno 1983). Once parcels are lifted above the core of the mesocyclone, the direction of the pressure perturbation force reverses to become downward-

TABLE 1. Characteristics of the four arrayed radars in the present analysis of the 6–7 Apr 2018 Monroe supercell. The NOAA P-3 airborne radars TFOR and TAFT operated in dual-PRF (extended Nyquist) mode, while SR1-P and KULM operated in single-PRF mode. An asterisk following a radar name denotes a polarimetric radar.

Radar	Wavelength (cm)	Half-power beamwidth (°)	Beam resolution (°)	Nyquist velocity (m s^{-1})	Max range (km)
TAFT	3.2 (X-band)	2.0	1	49 (extended Nyquist)	48
TFOR	3.2 (X-band)	2.0	1	49 (extended Nyquist)	48
SR1-P*	5 (C-band)	1.5	1	24	83
KULM*	10 (S-band)	1	1	28	135

directed in opposition to thermal buoyancy. In high-CAPE supercells, the upward buoyant acceleration dominates this negative dynamic acceleration and the parcel continues to gain updraft speed as it rises into the upper levels of the storm. In HSLC supercells, however, the maximum updraft speed occurs in the midlevels as the downward dynamical perturbation pressure force tends to dominate buoyancy (WP21). In addition, while a typical Great Plains long-lived supercell features a steady-state updraft, HSLC supercells feature a "pulse-like" evolution with discrete, intense upward pulses superimposed on the broader storm-scale updraft field, resulting in an updraft structure resembling the "weak evolution" scenario of Foote and Frank (1983) as applied by WP21.

To better understand the source and role of the SVC and the updraft structure of a supercell in the Southeast United States, a multiradar analysis of a tornadic supercell near Monroe, Louisiana (the "Monroe supercell"), on 6 April 2018, observed during the Verification of the Origins of Rotation in Tornadoes Experiment-Southeast (VORTEX-SE) 2018 field experiment, is presented. An array of four radars—one mobile ground-based research radar, one WSR-88D-equivalent fixed radar, and two NOAA P-3 airborne radars—sampled the supercell for over an hour at close range. Research soundings and the downward-pointing compact Raman lidar (CRL) system on the P-3 aircraft sampled the storm's thermodynamic environment. Diabatic Lagrangian analysis (DLA; Ziegler 2013a,b; DiGangi et al. 2016) was used to retrieve thermodynamic information along air parcel trajectories, enabling a full 4D high-resolution kinematic and thermodynamic analysis that is unprecedented in the Southeast.

This study will focus on two main questions: 1) What is the structure of the supercell's SVC, and how does it relate to the evolution of the supercell? and 2) How does the structure and evolution of the supercell's updraft compare to previous observed and simulated storms in the Southeast region and HSLC environments? Section 2 describes the data sources and analysis methods (the latter detailed in appendixes A–C), while section 3 overviews the storm case. Sections 4 and 5 present results and discussion, while section 6 offers concluding remarks.

2. Methods

a. Ground-based and airborne radars

A total of four radars (one ground-based mobile, one fixed, and two airborne; Table 1) provided simultaneous, full-volume Doppler observations of the 6–7 April 2018 Monroe supercell and neighboring deep convection (Fig. 2). The Shared Mobile Atmospheric Research and Teaching Radar 1 (SMART-R1 Polarimetric or SR1-P) was operated by the third author (MIB) and his research team (Biggerstaff and Carrie 2019), while the University of Louisiana–Monroe (ULM) NEXRAD-equivalent radar (KULM)[1] in Monroe, Louisiana (Murphy et al. 2019), was operated by the fourth author (TAM) and his ULM research team (Murphy 2018a). Led by the second author (CLZ), a NOAA P-3 research aircraft (N42RF) operated two tail Doppler radars (TDRs) scanning vertically oriented 3-s sweeps, the TDR-aft (TAFT) and TDR-fore (TFOR) radars being oriented 20° aft and forward of the normal to the P-3 fuselage, respectively.

Airborne and ground-based radar data were optimally combined to generate 11 consecutive analysis volumes during the period from 2255 to 0005 UTC. The two ground-based radars performed initially time-synchronized scans at 20 tilt angles between 0.8° and 43.0°, each volume taking about 4 min to complete (Table 2). The P-3 flew 11 consecutive legs transecting the near-inflow region along the southwest flank of the Monroe supercell from 2254 UTC 6 April to 0007 UTC 7 April 2018 at an elevation of about 1 km (Fig. 2), carrying instruments recording radar and in situ thermodynamic data (Ziegler 2019a,b). The P-3 legs were roughly 5 min in average length (Table 2), with successive legs requiring a roughly 3-min reverse-track maneuver that maintained a setback distance of about 10 km from the storm. Radar data collected during turns were excluded due to wide and irregular azimuthal spacings of the individual sweeps caused by the associated large heading angle changes of the banking aircraft. Each 360° TDR sweep was completed in 3 s, representing successive vertical storm cross sections separated by about 360 m of horizontal distance given a nominal cruise speed of up to about 115 m s^{-1}. The P-3 volumes were optimally matched to the ground-based radar volumes by choosing nominal volume analysis times that minimized time-to-space storm-advective gate location adjustments of both the ground-based radars in lower levels and the intersecting fore and aft TDR beams in the storm core region (Table 2).

b. Radar data editing

The editing procedures differed somewhat between the ground-based radars (KULM and SR1-P) and the airborne radars (TAFT and TFOR) due to their different technical

[1] Although KULM is not part of the NEXRAD network, its main operating characteristics (e.g., polarimetric, wavelength, frequency, half-power beamwidth, resolution) are comparable to a NEXRAD radar.

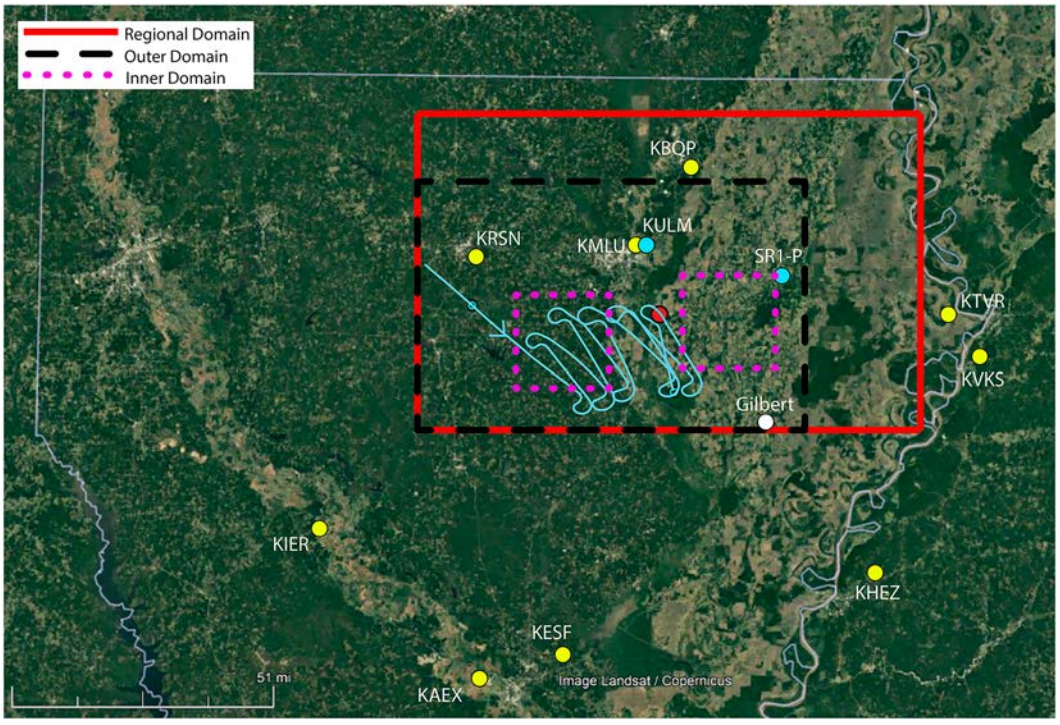

FIG. 2. Locations of observation platforms and radar analysis domain boundary rectangles (regional, red solid; outer, black dashed; moving inner at initial and final locations, purple dotted) employed in the 6–7 Apr 2018 study. Presented results concentrate on the outer and inner domains. Platform locations include ground-based radars KULM and SR1-P (blue dots), the Gilbert proximity sounding (white dot), and the flight track of the P-3 (blue line; arrow denoting P-3 motion). Available surface observation station locations are denoted by the yellow dots. The red dot locates the formation location of the EF-0 tornado associated with the Monroe supercell. The Monroe proximity sounding was near KULM. Note that the P-3 traversed over the former tornado location between legs 9 and 10. The inner domain moved with the storm motion vector. The first and last inner domains are denoted by the western and eastern purple boxes, respectively.

specifications and scanning techniques. Rotation corrections for "northing" the mobile SR1-P sweeps were deduced by correlating tall tower echoes with known tower locations via the Unidata Interactive Data Viewer (IDV) package (e.g., Ziegler 2013b) and implemented via the NCAR SOLOII software (Ziegler 2013b). Aircraft motion was removed from TDR velocity data using SOLOII, and ground clutter was detected and removed from both ground-based radars via a 3D spatial statistical clutter map generated using series of clear-air scans (Miller et al. 2020). A heavily customized Python script utilizing functions from the ARM Radar Toolkit (Py-ART) (Helmus and Collis 2016) was used to perform the bulk of radar editing (Alford et al. 2022; Biggerstaff et al. 2021; D. Stechman 2021, personal communication), consisting mainly of noise removal, TDR dual-PRF processor error detection and correction (Alford et al. 2022), TDR main and sidelobe ground clutter

TABLE 2. Radar volume time intervals for all four radars at each analysis time on the outer and inner domains. Note that TDR volumes are defined by the length of the leg. Successive analysis times are at irregular intervals due to the variability in timing of TDR legs. While utilizing all analyses, this study will primarily focus on 2335, 2343, and 2352 UTC, denoted by the italics.

Analysis time (UTC)	KULM	SR1-P	TAFT	TFOR
2255	2255:02–2259:21	2255:06–2259:34	2249:03–2255:34	2249:03–2255:35
2300	2300:02–2304:21	2300:06–2304:34	2258:42–2301:48	2258:42–2301:49
2307	2305:07–2309:35	2305:05–2309:35	2304:48–2308:27	2304:48–2308:28
2315	2315:02–2319:21	2315:06–2319:04	2311:54–2315:46	2311:54–2315:47
2322	2320:02–2324:21	2320:13–2324:41	2319:33–2323:20	2319:33–2323:21
2330	2330:02–2334:21	2330:06–2334:34	2326:57–2329:44	2326:57–2329:45
2335	*2335:02–2339:21*	*2335:06–2339:34*	*2332:42–2337:52*	*2332:42–2337:53*
2343	*2340:02–2344:21*	*2340:06–2344:34*	*2341:29–2345:00*	*2341:29–2345:01*
2352	*2350:02–2354:21*	*2350:06–2354:36*	*2349:02–2353:14*	*2349:02–2353:15*
0000	0000:02–0004:21	0000:07–0004:35	2356:30–0000:02	2356:30–0000:03
0005	0005:02–0009:21	0005:07–0009:35	0002:03–0006:40	0002:03–0006:41

TABLE 3. The times, dimensions, and number of passes of each objectively analyzed grid domain. All domains have grid spacings of 250 m × 250 m × 250 m in all directions, and also share the same grid levels and common grid points. The merged domain comprises the two-pass inner domain placed within the larger one-pass outer domain.

Domain name	Analysis time (UTC)	Domain size	No. of passes
Outer	2255–0005	120 km × 80 km × 14 km	1
Inner	2255–0005	30 km × 30 km × 14 km	2
Merged outer/inner	2255–0005	120 km × 80 km × 14 km	1 (outer), 2 (inner)

detection and removal, and dealiasing using a region-based algorithm and the proximity sounding wind profile. After the conclusion of bulk editing via the Py-ART script, all radar data were manually inspected and any additional dealiasing or ground target removal was performed with SOLOII. Dealiasing was essentially unnecessary for the P-3 TDRs in the present storm case, due to their large extended Nyquist velocity relative to ambient environmental wind shears (Table 1). Particular care was taken in both the automated and manual editing procedures to remove main- and sidelobe ground clutter contaminations, while otherwise preserving near-surface meteorological observations in both precipitation and clear air.

c. *Single-radar objective analysis and grid domains*

A spatial single-radar analysis based on multipass application of a 3D Barnes interpolation scheme (Barnes 1964; Koch et al. 1983; Majcen et al. 2008; Ziegler 2013b) was employed to map single-radar data to the analysis grid after time-to-space data position adjustment with storm motion (e.g., Ziegler 2013b). The spatial Barnes weighting function takes the following form:

$$\omega_{jk,n} = \exp\left(-\frac{r_{jk}^2}{\kappa_0 \gamma^{n-1}}\right), \tag{1}$$

where r_{jk} (km) is the distance from the jth grid point to the kth radar gate measurement, n is the pass number ($n = 1, N$), κ_0 (km^2) is the smoothing parameter of the first pass, $\gamma = 0.3$ is the convergence parameter, κ_0 (km^2) = $(1.3333\Delta)^2$ provides an estimate of the appropriate smoothing parameter value, and Δ (km) approximates the coarsest data spacing in the storm analysis volume (Koch et al. 1983; Majcen et al. 2008). Since radar gates are closely spaced in range and since interpolation effects a weighted average of all gates within the spherical influence volume centered on a gridpoint, the relatively fine radial data spacing allows Δ to be somewhat smaller than the coarsest azimuthal spacing in the storm. The radar objective analysis "resolution" is not determined by grid spacing—rather, by the combination of the radar gate spacing and wavelength-dependent amplitude response function corresponding to the chosen multipass Barnes filter function parameters.

A novel feature of the present study is the application of two different analysis grid domains ("outer domain" or "OD," and "inner domain" or "ID"; Table 3) under the principle that employing a smaller, nested domain with lateral boundaries closer to the networked radars allows a commensurately decreased minimum multipass κ value that maintains effective resolution of the coarsest (longest-range) radar observations in that particular domain (e.g., Skinner et al. 2014). By analogy to conventional nested-grid cloud-mesoscale models, nesting the ID single-radar analyses within their OD analysis domains takes advantage of the finescale Monroe supercell analysis within the broader coverage of the less well resolved field of other supercells and mesoscale convection at greater ranges in the Monroe supercell's meso-β-scale environment. The one-pass smoothing parameter $\kappa_0 = \kappa_{OD}$ (km^2) results in a degree of smoothing that retains the finest features resolved by the farthest (i.e., coarsest) storm radar observations in the OD, while the second-pass smoothing parameter $\kappa_{ID} = \kappa_{OD}\gamma$ (km^2) results in the smallest degree of smoothing necessary to fully resolve all (closer-range) storm radar observations in the ID. Both the ID and OD employ the first-pass smoothing parameter κ_{OD}, while the ID employs a second pass with κ_{ID}. Both analysis domains have a spatial grid separation of 250 m × 250 m × 250 m. Maintaining the same grid spacing for all domains enables domain mergers (see below) while preserving consistent spatial interpolation truncation errors for parcel trajectories as they cross domain boundaries (see section 2e and appendix A).

The smoothing parameter κ_0 for each analysis time was calculated following Pauley and Wu (1990) and based on the distance from KULM to the Monroe supercell, and this time-dependent κ_0 was applied to all four radars (Table 4). This

TABLE 4. The κ_0 values at each analysis time, as constrained by distance of the Monroe supercell storm core region from KULM. Azimuthal data spacing Δ for KULM and SR1-P are calculated from the small angle approximation for 1° beam resolution (Table 1). The maximum range restriction imposed on SR1-P based on the constrained κ_0 is shown for each analysis that includes SR1-P. As in Table 2, italics denote the three analysis times primarily shown in this study.

Analysis time (UTC)	Storm core region distance from KULM (km)	Smoothing parameter $\kappa_0 = \kappa_{OD}$ (km^2)	Maximum range of SR1-P (km)
2255	41	0.907	—
2300	38	0.779	—
2307	35	0.661	—
2315	30	0.485	—
2322	26	0.365	—
2330	23	0.285	—
2335	*22*	*0.261*	—
2343	*21*	*0.238*	—
2352	*22*	*0.261*	*22*
0000	26	0.365	26
0005	28	0.423	28

TABLE 5. Detailed description of and citations related to the four steps of the multiradar velocity synthesis procedure.

Synthesis step	Description	Variables	Citations
1) Anelastic mass continuity integration	1.1) Downward iterative integration of two linear normal equations and anelastic mass continuity equation from $w = 0$ at storm top 1.2) Bulk fall speed V_t from empirical function of reflectivity	u, v, w, V_t	Kessinger et al. (1987), Ziegler (2013b)
2) Hole filling missing grid points	2.1) Missing gridpoint wind components filled from gridded environmental sounding ($w = 0$) 2.2) Multiple passes of nine-point 2D horizontal filter applied to filled winds using fixed radar-synthesized (u, v, w) wind components as lateral boundary conditions	u, v, w	Ziegler (2013b); Haltiner (1971)
3) O'Brien adjustment	3.1) O'Brien column adjustment via anelastic mass continuity constrains integrated divergence to vanish with $w = 0$ at surface and domain top 3.2) Adjusted 3D w field is horizontally smoothed with sixth-order filter	w	O'Brien (1970); Raymond (1988)
4) 3D variational adjustment	3D variational adjustment of all wind components is performed by applying anelastic mass continuity as a strong constraint spanning the full domain	u, v, w	Ray et al. (1978) [their Eqs. (16)–(19)]

approach minimized unnecessary smoothing when the Monroe supercell was closer to the array of radars. A maximum single-radar analysis range was determined from this calculated κ_0 for SR1-P, and SR1-P was excluded from all analysis times where its maximum analysis range did not reach the ID (Table 4). The single-radar ID objective analyses of KULM, TAFT, and TFOR were inserted within their respective OD analyses at each analysis time, with horizontal, multipass application of a five-point elliptic filter (Haltiner and Williams 1980) within a narrow "sponge zone" along and near the ID lateral boundaries to locally preserve spatial continuity. In contrast, SR1-P was only analyzed on the OD (i.e., with no ID analysis or subsequent insertion into the OD) due to that radar's larger range from and broader physical beamwidth within the supercell. Since the radially uniform TDR along-track data spacing of about 0.35 km would justify a constant $\kappa_0 = 0.217$, it was necessary to concede effective overfiltering of the TDR data via the utilized range-constrained κ_0 values to conduct airborne/ground-based multiradar analysis of this case.

d. Multiple-Doppler velocity and reflectivity synthesis

An "over-determined dual-Doppler" radar synthesis algorithm (Ray et al. 1980; Ray and Sangren 1983; Kessinger et al. 1987; Ziegler 2013b) was applied to synthesize the merged-domain single-radar objective analyses described in section 2c (Tables 2–4). The synthesis of vector velocity $\mathbf{V} = u\hat{\mathbf{i}} + v\hat{\mathbf{j}} + w\hat{\mathbf{k}}$ (i.e., where u, v, and w are the west–east, south–north, and vertical velocity components, respectively) followed a multistep algorithm that combined gridpoint radial velocities from up to four radars (as described in section 2a) via the system of two normal (overdetermined) equations for the u and v components with the anelastic mass continuity equation[2] (Table 5). The reflectivity synthesis was determined from the maximum single-radar reflectivity value from any radar at each grid point. All four radars, being individually well-calibrated, generally had reflectivities within 5 dB of each other where the X- and C-band radars were unattenuated. Since KULM's objectively analyzed S-band gridded reflectivity was essentially unattenuated, assigning the maximum reflectivity value among the X-, C-, and S-band radars thus effectively mitigated attenuation effects in the gridded reflectivity field. The radar synthesis algorithm excluded all KULM/SR1-P dual-Doppler pairings at any given analysis time, since such pairings occasionally produced nonphysical velocity artifacts due to the narrower KULM pencil beam at close range more accurately measuring the vertically sheared low-level winds than the broader SR1-P beam at longer range. Derived kinematic fields including asymptotic contraction and fluid trapping (Cohen and Schultz 2005), vertical vorticity, horizontal storm-relative streamwise vorticity, and 3D deformation were calculated from the 3D wind fields.

e. Diabatic Lagrangian analysis, compact Raman lidar, and vorticity trajectory calculations

Diabatic Lagrangian analysis (DLA), a kinematic thermal-microphysical continuity retrieval of heat and water substance based on integration of ordinary differential conservation equations of heat and water substance along Lagrangian trajectories that terminate at analysis grid points and proceed from a series of input time-varying 3D wind and reflectivity analyses (Ziegler 2013a,b), has been applied to map the thermal and hydrometeor fields in the Monroe supercell. The DLA builds upon an earlier thermal–microphysical continuity retrieval method based on a solution of a parabolic system of conservation equations for heat and water substance (e.g., Ziegler 1985, 1988), an earlier application of Lagrangian retrieval of thermodynamic parameters (Knupp 1996), and previous refinement and application of the DLA (DiGangi et al. 2016; Miller 2018; Chmielewski et al. 2020; Miller et al. 2020). Diagnosed fields include the precipitation mixing ratios of rain (q_r), graupel/hail (q_g), and snow (q_s), while predicted

[2] Although a vertical vorticity constraint could generally help improve airflow consistency (e.g., Potvin et al. 2012), the present overdetermined multi-Doppler velocity synthesis provides sufficient analysis robustness.

fields include potential temperature (θ) and mixing ratios of water vapor (q_v), cloud water (q_c), and cloud ice (q_i). Additional thermodynamic variables including temperature, virtual temperature (T_v) and virtual potential temperature (θ_v), equivalent potential temperature (θ_e), dewpoint temperature, and relative humidity (RH) are derived from the Bolton (1980) formulas. The 35 km × 35 km × 14 km DLA domain has been positioned within the merged radar analysis domain (with coincident radar and DLA grid points) to follow the Monroe supercell motion. Details of the DLA formulation are presented in appendix A.

The downward-pointing compact Raman lidar (CRL) instrument (Liu et al. 2014; Wang et al. 2016) was deployed on the P-3 during VORTEX-SE (Lin et al. 2023), profiling air temperature, water vapor mixing ratio (q_v), and lidar scattering ratio (LSR) with a vertical grid spacing of 1.2 m and a horizontal grid spacing of 360 m. A quality-controlled, smoothed version of the CRL data has been analyzed during the 10 legs of the P-3 that transected the near-inflow of the Monroe supercell during the period 2249–0006 UTC (Fig. 2, Table 2). The CRL provides high-resolution near-inflow thermodynamic measurements within 30 km of the storm. Although the "proximity" Gilbert, Louisiana, sounding (Murphy 2018b) provides a reasonable approximation of the deep-tropospheric regional-scale thermodynamic environment, the CRL results inform modifications of the boundary layer (BL) thermodynamic profile used in the initialization of air parcels in the DLA (as described in appendix A and section 3). Details of the CRL data analysis are presented in appendix B.

Vorticity dynamical equations (e.g., Brandes 1983, 1984; Roberts et al. 2016) have been integrated forward in time along selected DLA trajectories to determine predicted parcel vector vorticity and vorticity source tendencies at Lagrangian points. Both the initial parcel vorticity and the relevant time-dependent radar-analyzed and DLA-retrieved forcing fields are precalculated as needed and interpolated to the individual Lagrangian points to assist integration. Details of the vector vorticity calculations are presented in appendix C.

3. Case overview

The 6–7 April 2018 VORTEX-SE deployment (IOP 4) had dual objectives to sample a mesoscale convective system (MCS) over northeastern Louisiana in the late evening and also sample supercells south of the developing MCS in the late afternoon should they develop. Multiple supercells formed in the late afternoon in this region, including one isolated tornadic supercell (the "Monroe supercell"), which is the focus of this study.

A lee cyclone over north-central Texas induced a warm front which pushed north to the Louisiana–Arkansas border before stalling into a stationary front. Strong southerly winds in the warm sector south of this front enabled significant moisture advection to northern Louisiana. A modest elevated mixed layer (EML) advected from the west-southwest injected a shallow layer of steep midlevel lapse rates above the warm, moist BL, facilitating ~1900 J kg^{-1} of mixed-layer (ML) CAPE by late afternoon (Fig. 3), double the MLCAPE typically associated with HSLC supercells (e.g., WP21).

The Storm Prediction Center (SPC) issued an Enhanced risk (level 3 of 5) for severe thunderstorms from east Texas through western Mississippi for this event. While the primary risks anticipated were severe winds associated with the MCS, the forecast noted a conditional tornado threat with any semidiscrete storms due to strong low-level shear and sufficient hodograph curvature in northern Louisiana (Fig. 3c).

Surface heating, BL mixing, and continued moisture advection overcame the stable EML by late afternoon. The Monroe supercell initiated at approximately 2220 UTC about 20 km south of Ruston, Louisiana, just south of another mature supercell. While multiple supercells and tornadoes occurred during this event, the Monroe supercell was the only supercell in northeast Louisiana to produce a tornado. By 2300 UTC, the Monroe supercell was the dominant storm in the region and its inflow had uninhibited access to the open warm sector. Other earlier supercells had either merged together in the initial forming of the developing MCS, or were weakening likely due to their inflow being cut off by the outflow of nearby storms.

The Monroe supercell produced an NWS-surveyed EF0 tornado about 23 km to the southeast of Monroe, Louisiana, that was on the ground during the period 2340–2353 UTC and traveled approximately 12.6 km with an estimated maximum path width of 46 m (NOAA NCEI Storm Events Database, https://apps.dat.noaa.gov/StormDamage/DamageViewer/). Due to this area being forested and lightly populated, the NWS survey team noted only four EF0 damage points. In addition, the survey team assessed an EF1 damage point slightly off-track from the EF0 tornado at 2355 UTC (2 min after the end of the EF0 tornado). By 0000 UTC, the structure of the Monroe supercell had degraded as it interacted with convection to its north and east, and after 0005 UTC it could no longer be identified as a supercell as it merged with the developing MCS.

The 2234 UTC Gilbert sounding (Figs. 3a,c) was the designated proximity sounding. While positioned within the broad, open region of southerly flow, it was ~50 km away from the Monroe supercell and launched an hour before the analyses presented here. Although the 2231 UTC Monroe sounding (Figs. 3b,d) was closer to the storm, collocated surface station data and radar showed that its environment was contaminated by previous convection in the area and the convectively reinforced stationary front, which was sagging southward (Hosek 2022). The time-varying leg-averaged CRL profiles (Fig. 4) were applied to modify the low-level, near-inflow thermodynamic profile of the Gilbert sounding. While horizontal intra-leg heterogeneity on the order of 1–2 K and 1 g kg^{-1} was present (Hosek 2022), exploring the influence of this variation within the supercell inflow was beyond the scope of this study. Nonlinear parametric thermodynamic profiles of q_v and θ from the surface to 1 km were qualitatively fit to the BL profiles measured by the proximity sounding, the 2234 UTC Monroe sounding, the CRL measurements, and in situ measurements from regional surface stations and the P-3, while other variables were derived using Bolton's (1980) formulas. The parametric vertical profile of thermodynamic variable $\phi(z)$ in the lowest 1 km takes the form:

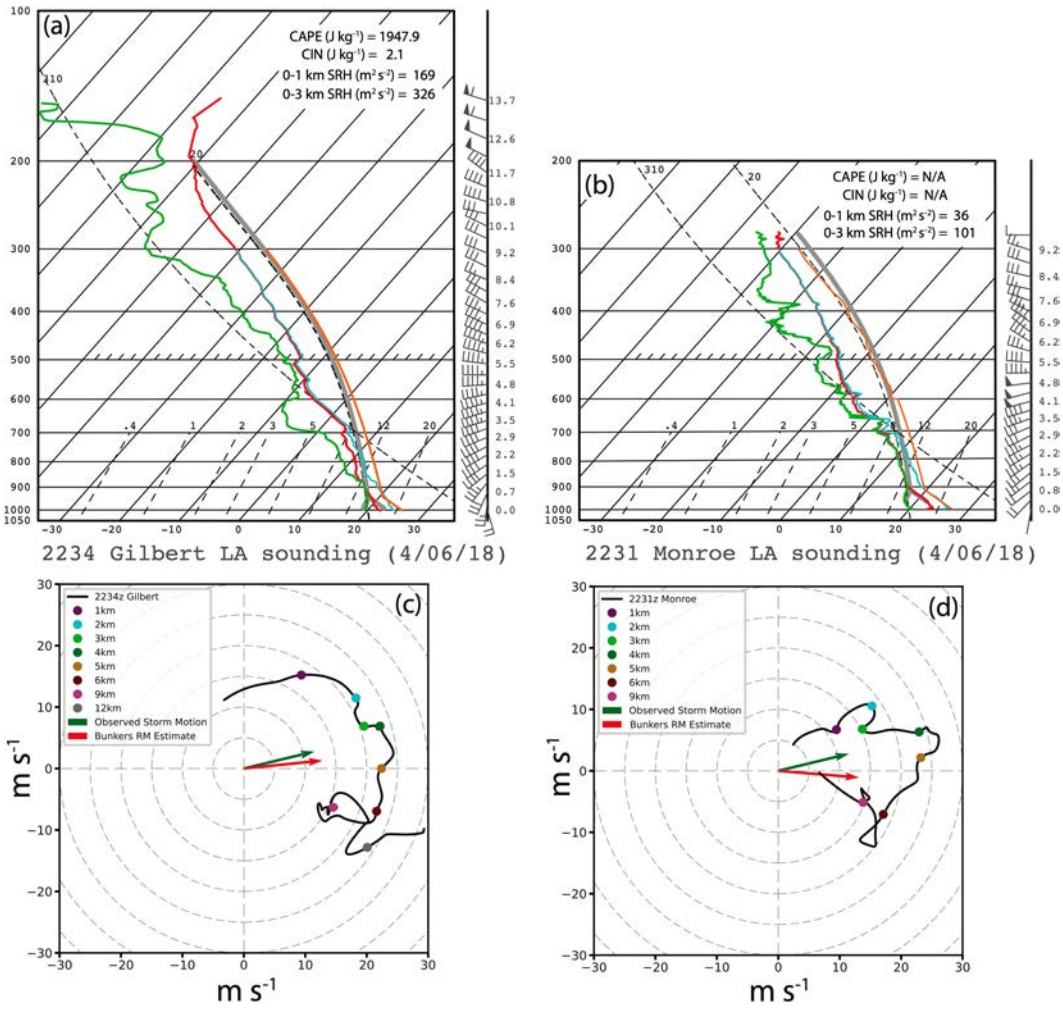

FIG. 3. Observed soundings in northeastern Louisiana on 6 Apr 2018. (a),(c) The 2234 UTC Gilbert sounding and hodograph; (b),(d) the 2231 UTC Monroe sounding and hodograph. Dry adiabats and isohumes of an adiabatically lifted surface-based, boundary layer averaged parcel are shown in gray up to the LCL, and the moist adiabat for the same parcel is shown in gray above that. Cyan and orange curves are the sounding and lifted-parcel virtual temperature profiles, respectively. Colored dots on the hodographs denote heights above the surface, with observed storm motion denoted by the green arrow and Bunkers right motion denoted by the red arrow. Storm-relative helicity (SRH) is calculated using the observed storm motion.

$$\phi(z) = \phi_{\text{sfc}} + \left(\frac{\Delta\phi}{\Delta z}\right)_{1\text{km}} z + \Delta\phi_{\text{sfc}} e^{-(z/z_0)}, \tag{2}$$

where z (m) is height, ϕ_{sfc} is the linear profile function value at the surface, $(\Delta\phi/\Delta z)_{1\text{km}}$ is the vertical gradient of the linear profile function between the surface and 1 km, $\Delta\phi_{\text{sfc}}$ is the excess surface value relative to ϕ_{sfc}, z_0 (m) is the e-folding vertical scale of the asymptotic inverse-exponential deviation from the linear profile, and $\Delta z = 1000$ m. The thermodynamic variables at the 1.25-km level were derived by averaging the 1-km CRL-derived value and the 1.5-km Gilbert sounding value, while above 1.5 km the thermodynamic profile was prescribed directly from the Gilbert sounding. This hybrid thermodynamic profile was used to thermodynamically initialize the DLA trajectories. Surface in situ measurements were subjectively given the least weighting as five of the nine available stations were located north of the stationary front during the analysis period or were influenced by other convection, while the remaining four stations were ~120 km south of the Monroe supercell (Hosek 2022). Neither subdivision of the available surface measurements were ideally placed for sampling the Monroe supercell inflow environment.

4. Results

a. *Internal boundary identification criteria*

Internal storm boundaries in the Monroe supercell are identified in the surface θ'_v and analyzed wind fields. The LFCB and FFCB are drawn along the leading (warm) edge of a thermodynamic boundary defined by a θ_v gradient. The

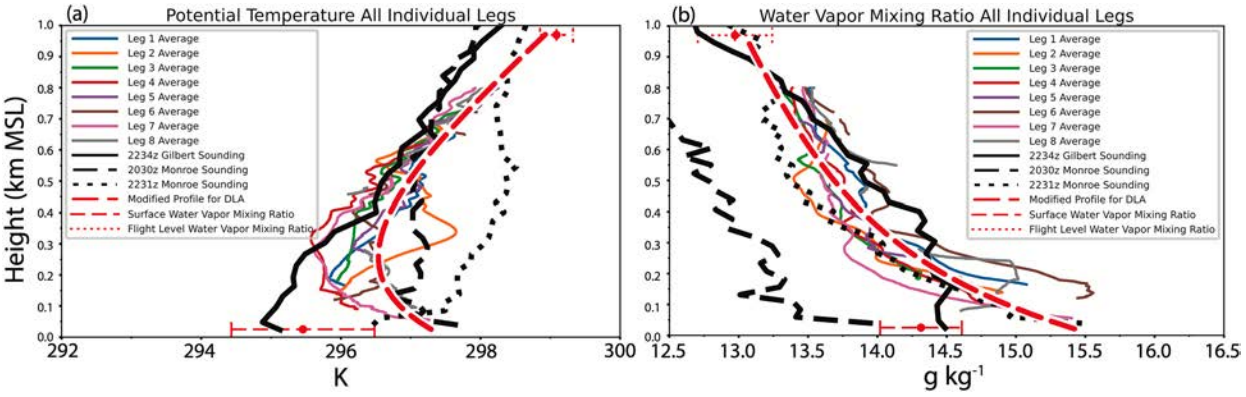

FIG. 4. Comparison of leg-averaged vertical CRL-derived profiles from the first eight P-3 legs against in situ measurements (see legend for depiction of each measurement) of (a) potential temperature and (b) water vapor mixing ratio. Thin colored curves denoting the CRL profiles are compared to the 2030 UTC Monroe sounding (dashed black), 2231 UTC Monroe sounding (dotted black), and 2234 UTC Gilbert sounding (solid black). Regional surface observation values are denoted by the average (red dot) and ±1 standard deviation (red dashed line). P-3 flight-level in situ values at the average elevation spanning the analysis period are denoted by the average (red dot) and ±1 standard deviation (red dotted line). The thick red dashed profile represents the parametric 0–1-km vertical profile [see Eq. (2) in the text], informed by the above measurements, that has been used to initialize the DLA.

FFCB, being defined as a relatively weak thermodynamic boundary between the inflow and diabatically cooled air (BW13), is defined in this study as a θ_v gradient of roughly 0.5 K km^{-1} compared to the inflow and located in the forward flank of the storm. The LFCB, being thermodynamically stronger than the FFCB (BW13), is defined as a θ_v gradient of roughly 1 K km^{-1} and located internal to the storm relative to the FFCB and sited along the leading edge of the forward-flank downdraft. Confluence of surface flow is used to further confirm the θ_v gradient representing the boundary, particularly for the LFCB as it is extended into the forward-flank precipitation region. The classification of the FFCB and LFCB is further discussed in section 5a.

The RFGF is drawn along the leading edge of a θ_v gradient of at least 0.5 K km^{-1} in the rear flank of the storm. If a gust front feature is present in the wind field absent the prescribed thermodynamic gradient, the RFGF is drawn along the leading edge of the gust front. A rear-flank internal surge (RFIS) is defined if a thermodynamic gradient matching that defined above for the RFGF is present behind, and distinctly separate from, a gust front-defined RFGF.

Once a boundary is defined, it is maintained spatially and temporally along a consistent θ_v' isotherm barring changes in storm structure noted from a change in confluence zones in the surface wind pattern. Portions of isotherms associated with identified boundaries that do not meet the above criteria, yet visual evidence is present of an increasing θ_v gradient along flow direction, are denoted as "weak" or "developing" boundaries.

b. *Evolution of storm boundaries and identification of an SVC*

The Monroe supercell maintained a quasi-stationary reflectivity structure before 2335 UTC (e.g., as in Fig. 5a). Despite the east-northeasterly motion of the supercell main updraft and mesocyclone along the thin dashed line in Fig. 5, its forward anvil precipitation region extends southward due to strong storm-relative northerly flow aloft (Fig. 3c). This differs from "traditional" conceptual diagrams of supercell structure, which feature relatively backed low-level storm-relative winds with west-southwesterly winds aloft which push the forward anvil precipitation to the east-northeast ahead and to the left of supercell motion (e.g., Fig. 1). A westward-trailing RFGF extends from the inflow notch of the emerging hook echo. The rear-flank downdraft (RFD) can be identified by the intense warm pocket of θ_v' just north of the RFGF at 500 m (Fig. 5d, x = 70 km, y = 47 km), the result of compressional warming from a downdraft (not shown due to weakness at 500 m, but evident at higher elevations of the storm at this location). This is collocated with a surface storm-relative northerly wind associated with cooled air (Fig. 5c). A southward-recurving FFCB (BW13; S21; see also discussion of internal boundary naming convention in section 5a) with marginal baroclinity and only weak low-level confluence extends roughly along the reflectivity gradient from the inflow notch and low-level updraft south-southeastward along the western edge of the forward anvil precipitation region (Figs. 5a,c). Since the supercell inflow is traversing over land recently under the forward anvil precipitation region, it is possible that surface fluxes of moisture and cooling associated with diabatic processes are diminishing the baroclinity of the FFCB. The consequences of this low-level inflow modification with regards to supercell intensity and organization, while intriguing, are outside the scope of this study.

Moderate streamwise vorticity locally exceeding 15×10^{-3} s^{-1} is evident on the cool side of the FFCB (Fig. 5b, x = 74.5 km, y = 46 km), but it is unclear if this is related to the baroclinity of the FFCB given its disorganization. In contrast, a spatially large swath of notable streamwise vorticity with a maximum of 25×10^{-3} s^{-1} is evident in the precipitation-free inflow leading into the low-level updraft. Its placement in the warm sector suggests that this streamwise vorticity is not baroclinically generated. It may be the result of

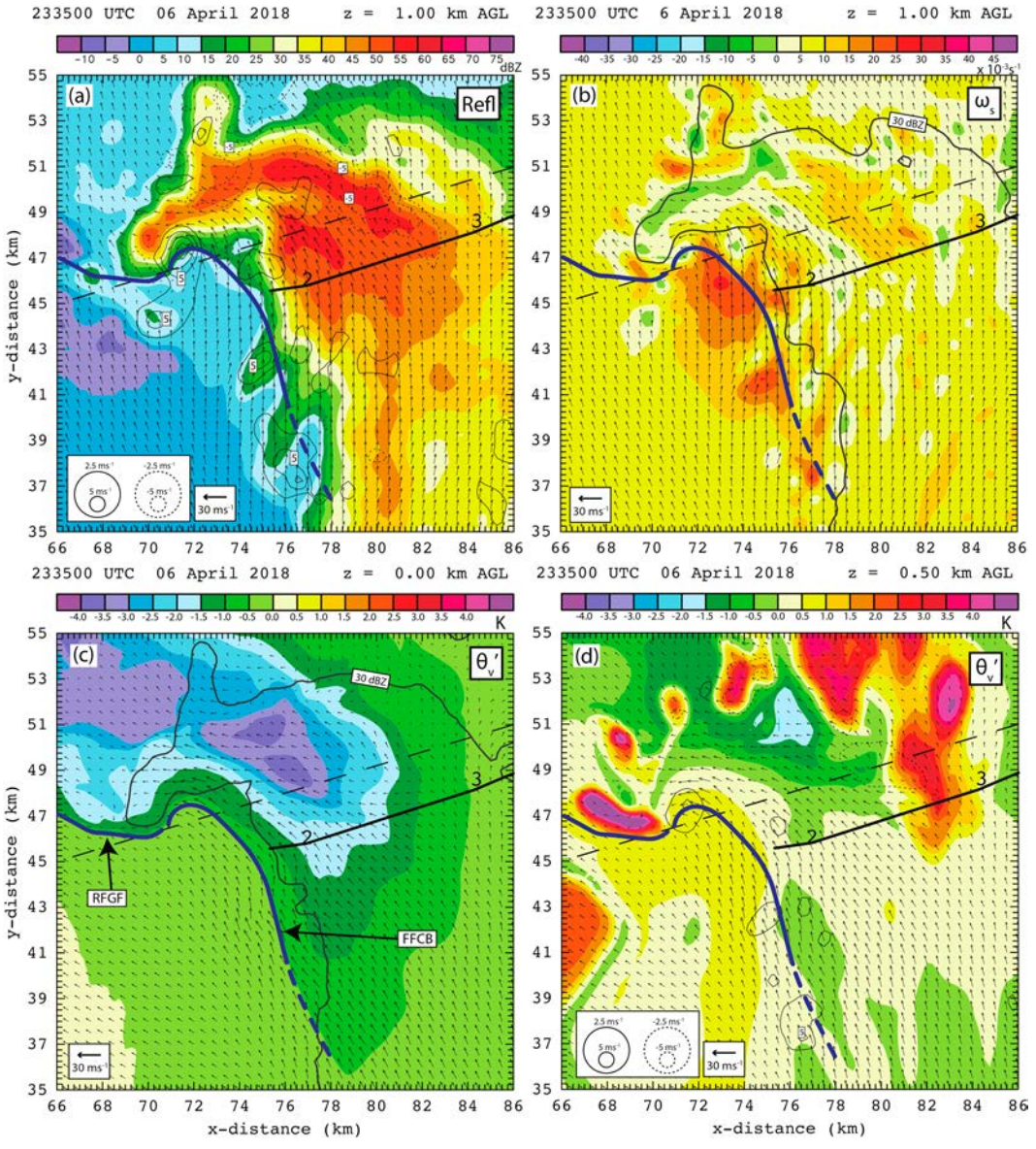

FIG. 5. Radar-analyzed and DLA-retrieved horizontal fields at 2335 UTC. (a) Reflectivity fill with contoured vertical velocity at 1 km (all contours and color fills are presented at the same height), (b) streamwise vorticity fill with 30-dBZ contour at 1 km, (c) virtual potential temperature perturbation θ_v' fill (i.e., the DLA-retrieved θ_v minus the input sounding θ_v at altitude) with 30-dBZ contour at the surface, and (d) θ_v' fill with contoured vertical velocity at 0.5 km. Airflow vectors are storm-relative. The solid black curve represents the NWS-surveyed EF0 tornado damage track, with number labels "2," "3," "4," and "5" (the latter two outside of the domain shown here) representing individual damage markers (note: damage marker "1" is a straight-line wind report upstream from the tornado track in an earlier analysis). The dashed black line denotes the location of the main supercell low-level mesocyclone at 2343 UTC projected forward and backward in time with the storm motion. Blue lines denote surface boundaries identified using surface θ_v' and the analyzed wind field (labeled in figure). Dashed blue lines denote surface boundaries that are weak or developing. The color-filled field is denoted in the top right of each panel, and contour labels are present for the 30-dBZ line and every other velocity interval.

horizontal stretching due to accelerations toward the low-level updraft, which is intensifying at this time ahead of tornadogenesis.

By 2343 UTC (about 3 min after tornadogenesis), the Monroe supercell has undergone significant structural changes (Fig. 6). The RFGF surged southward as the result of an apparent RFD surge, with a RFIS behind it. The solitary near-surface mesocyclone in the inflow notch of the emerging hook echo at 0.25 km increases from 15×10^{-3} s^{-1} at 2335 UTC (not shown) to double maxima of up to 15×10^{-3} and

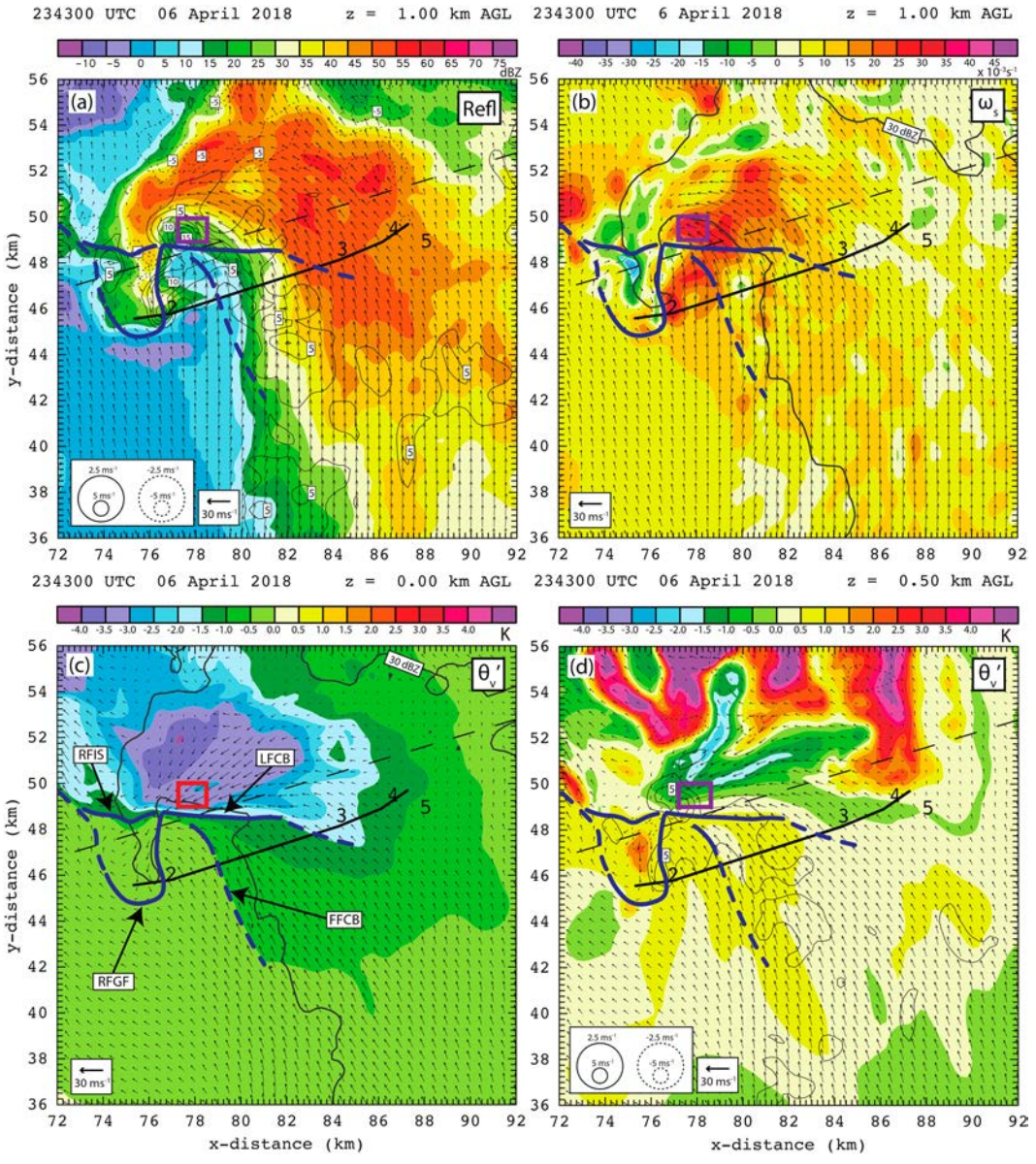

FIG. 6. As in Fig. 5 but at 2343 UTC, which is shortly after the estimated time of tornadogenesis. The purple box in (a), (b), and (d) and the red box in (c) denote the SVC location used for trajectory analysis (see section 4d).

30×10^{-3} s^{-1} at 2343 UTC (Fig. 7), the latter locating the tornado–cyclone in the "asc" (annular section of the cylinder) region (Garrett and Rockney 1962), which is indicative of reflectivity scatterers wrapping counterclockwise around the tight radar-analyzed cyclonic vortex at the tip of the hook echo. Similarly, the solitary low-level updraft in the weak-reflectivity inflow at 1 km also increases from 10 m s^{-1} at 2335 UTC (Fig. 5a) to double maxima of 10 and 15 m s^{-1} collocated with the asc region and inflow notch, respectively (Fig. 6a). The southern updraft collocated with the strong tornado–cyclonic vertical vorticity maximum bears some similarity to the occlusion updraft in the 29–30 May 2004 Geary, Oklahoma, supercell (Betten et al. 2018).

Of particular interest to this study are the internal storm boundaries and their associated corridors of streamwise vorticity maxima (Fig. 6). The west-northwest–east-southeast-oriented LFCB (BW13; S21; see also section 5a) extends from the triple-point under the main supercell updraft into the forward-flank precipitation and is characterized by a relatively sharp θ_v gradient of -3 K over 1-km horizontal distance at the surface at its strongest point (Fig. 6c). At 500 m, strong baroclinity is present ~1 km to the north of the LFCB, consistent with a roughly 30° northward tilt of the cold pool with height (Fig. 6d, $x = 78.5$ km, $y = 49$ km). Notable low-level confluence is also present along the LFCB. A confined corridor of streamwise vorticity broadly exceeding 25×10^{-3} s^{-1}

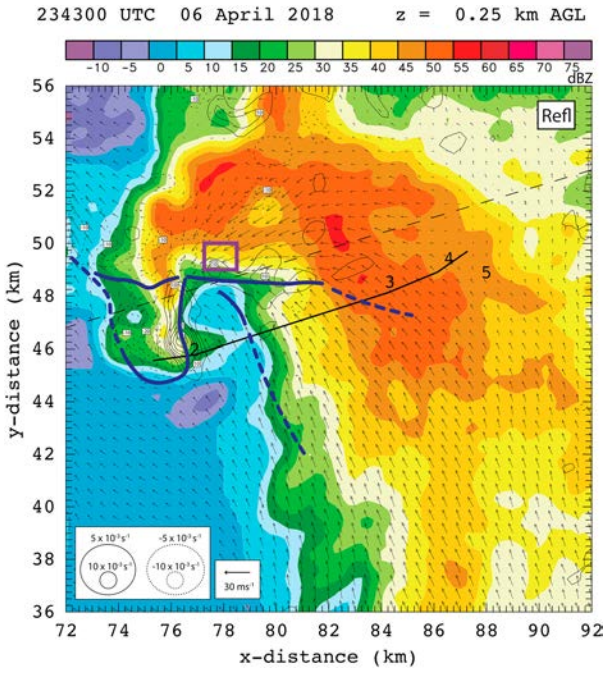

FIG. 7. Reflectivity fill with contoured vertical vorticity both at 0.25 km for 2343 UTC. Blue lines denote surface boundaries, and the purple box denotes the SVC location used for trajectory analysis (see Fig. 6). Airflow vectors are storm relative.

(5 times the base-state streamwise vorticity at 1 km) and up to 35×10^{-3} s^{-1} located along the cool side of the LFCB (Fig. 6b, $x = 78.5$ km, $y = 49$ km) is classified as an SVC. The 25×10^{-3} s^{-1} magnitude of streamwise vorticity threshold and its elongated appearance along the LFCB are consistent with previous (albeit perhaps somewhat arbitrary) definitions of an SVC (Murdzek et al. 2020; S21). The aforementioned FFCB extends southeastward from a triple-point junction having presumably been partially undercut by colder air behind the forming LFCB. While some vorticity maxima exceeding the threshold were present within the warm inflow and near the tornado–cyclone (Fig. 6b, $x = 76.75$, $y = 46$), these were not considered part of the SVC due to their location in the warm inflow.

The cold pool core and internal boundaries of the Monroe supercell shift downstream with respect to the low-level inflow toward the left of the main updraft and mesocyclone motion by 2352 UTC (Fig. 8). A wide swath of streamwise vorticity exceeding 25×10^{-3} s^{-1} with embedded maxima exceeding 45×10^{-3} s^{-1} is within the cold pool core and appears to lead into the low-level updraft (Figs. 8b–d, $x = 86.5$, $y = 51$). While this swath of streamwise vorticity is further displaced from the drawn LFCB than the SVC identified at 2343 UTC, the LFCB tilts northwestward with height, and a significant amount of the swath of streamwise vorticity can be collocated with the tightest baroclinic gradient at 0.5 km (Fig. 8d). The lack of available independent analyses between 2343 and 2352 UTC preclude a determination of the temporal consistency of this feature with the SVC at 2343 UTC. Despite this, its characteristics remain consistent with our definition of an SVC. The western end of the cold pool surged southwestward by this time, undercutting the main updraft and encroaching on the remnant low-level tornado–cyclone (Figs. 8c,d). The LFCB thus rotated counterclockwise as its western edge sagged southward along the leading edge of the gusting-out cold pool, potentially disrupting a favorable alignment for parcels not traveling deep within the cold pool to attain large streamwise vorticity. Despite being located further within the cold pool compared to 2343 UTC, the SVC is still present at 2352 UTC. The southward surge of the cold pool continued through 0000 UTC as the storm rapidly lost supercell characteristics and the SVC dissipated (not shown; Hosek 2022). Due to the significant storm structure evolution underway at 2352 UTC, further analysis of the SVC will be conducted at only 2343 UTC.

c. *SVC structure*

The slantwise vertical structure of the LFCB and its associated transient SVC is evident at 2343 UTC (Fig. 9). The cold pool of the Monroe supercell is about 1.25 km deep, and, due at least partially to the southward surge in cold air already underway by 2343 UTC, the baroclinic boundary has a northward tilt with height. Vertically stratified warm θ_v' above the LFCB is associated with condensation latent heat release within the cloudy supercell updraft, which tilted northeastward over the boundary (Fig. 9a). A horizontal nonclosed, rotor-like circulation is present in the radar-analyzed wind field through the DLA-retrieved baroclinic boundary, consistent with the hypothesis that the circulation is at least partially baroclinically forced (Fig. 9c, $x = 3.5$ km, height = 0.75). The horizontal circulation and its associated streamwise vorticity maximum is concentrated between 250 and 1500 m and maximized at 1000 m. A local vertical vorticity maximum of 10×10^{-3} s^{-1} is also along the leading edge of the LFCB (Fig. 9d).

d. *Trajectories through the SVC*

A subset of DLA trajectories in the Monroe supercell are analyzed to determine how parcels which passed through the SVC may have influenced the supercell. Fourteen trajectories from 2337 to 2352 UTC that passed through the SVC at 2343 UTC are selected for vorticity dynamical analysis (Fig. 10). The trajectories are required to be within the $(\Delta x, \Delta y, \Delta z)$ coordinate range (77.25–78.50 km, 49.00–50.00 km, 0.5–1.25 km) at 2343 UTC (denoted by the purple box in Figs. 6 and 10) to isolate trajectories passing through the SVC.

Eight of the 14 trajectories are located along or on the cool side of the LFCB at 2337 UTC (Fig. 10b). The remaining six trajectories originate to the southeast of the SVC on the warm side of the LFCB and feature varying degrees of turning as they approach and pass through the SVC (Fig. 10a). Only two of these remaining six parcels that originate from the southeast are located within 1 km of the FFCB (Fig. 10a). Most trajectories feature a significant easterly component within the SVC region favorable for long residence time within the baroclinic solenoidal circulation (Figs. 10a,b). After passing through the SVC, all parcels subsequently reach the main updraft and drift eastward in the tilted updraft

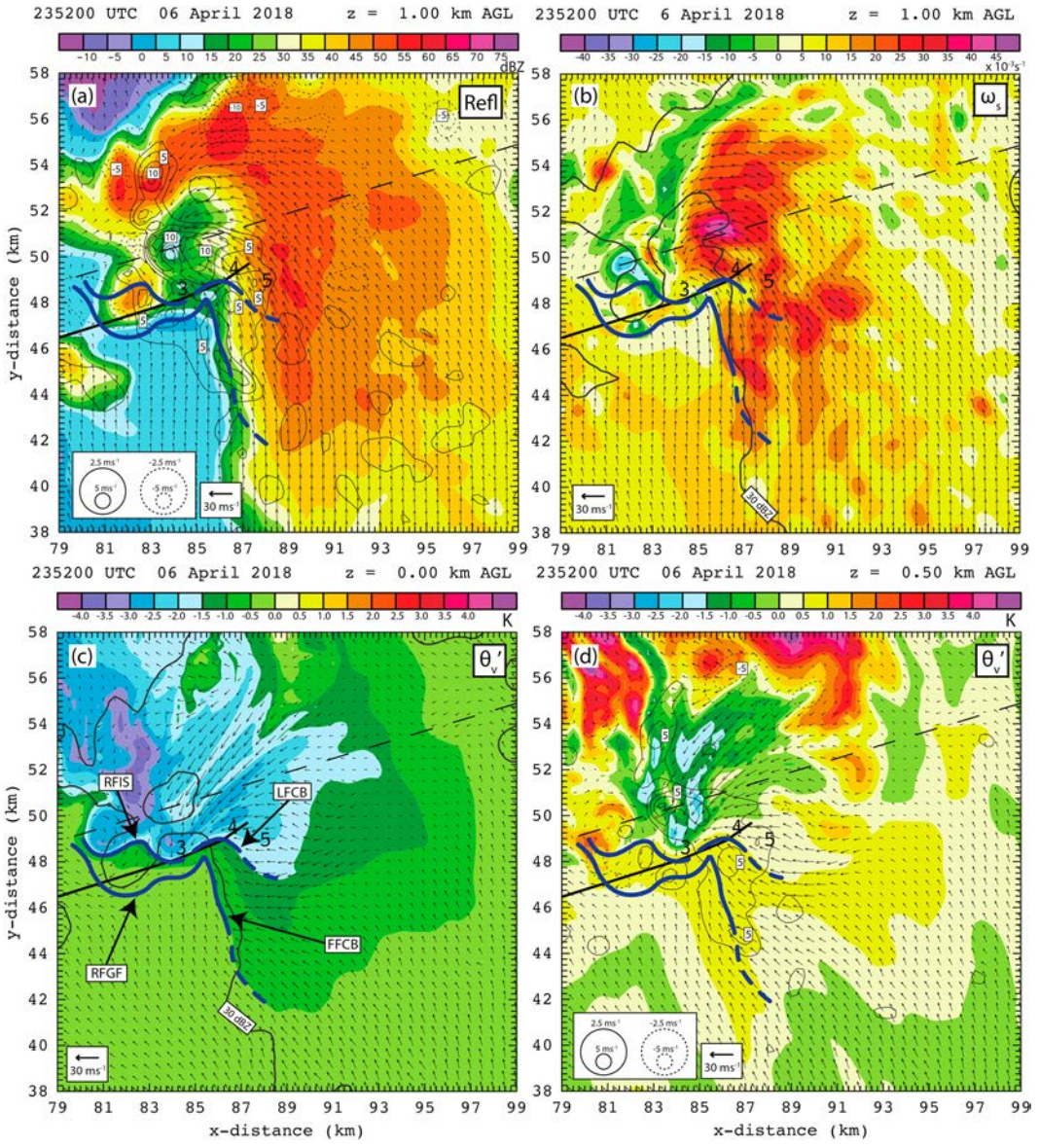

FIG. 8. As in Fig. 5, but at 2352 UTC.

(Figs. 10a–d). All parcels are between heights of 8 and 10 km in the storm updraft by 2352 UTC (not shown). *No trajectories which pass through the SVC region subsequently enter the tornado–cyclone*, which is located within a secondary updraft maximum at the southern tip of the reflectivity hook echo and approximately 2 km south of the main supercell updraft (Figs. 10a–d).

Two trajectories are selected to represent pathways through the designated SVC region at different angles, with one trajectory ("A") entering the SVC from the cold pool to the northeast, and the other ("B") entering from modified inflow to the southeast (Figs. 10c,d). The two representative trajectories are chosen from these two subset pathways [one from the cool side of the LFCB (Fig. 10b), one from the warm side of the LFCB (Fig. 10a)] as those with the lowest horizontal vorticity residual—the magnitude of the difference between the observed horizontal vorticity and horizontal vorticity predicted by the vorticity dynamical equations (see section 2e and appendix C)—prior to entering the updraft (Fig. 10f). The maximum residual magnitudes of the two representative trajectories prior to 2343 UTC are 8×10^{-3} and 10×10^{-3} s^{-1} for trajectory A and B, respectively, which are reasonably small compared to their maximum observed horizontal vorticity magnitudes of 20×10^{-3} and 33×10^{-3} s^{-1} for trajectory A and B, respectively (Fig. 10f).

Vorticity dynamical tendencies for the two representative trajectories are shown in Fig. 11. The tilting of horizontal streamwise vorticity and stretching of vertical vorticity provide the primary vertical vorticity forcing in all trajectories (not shown). Both representative trajectories have a noted

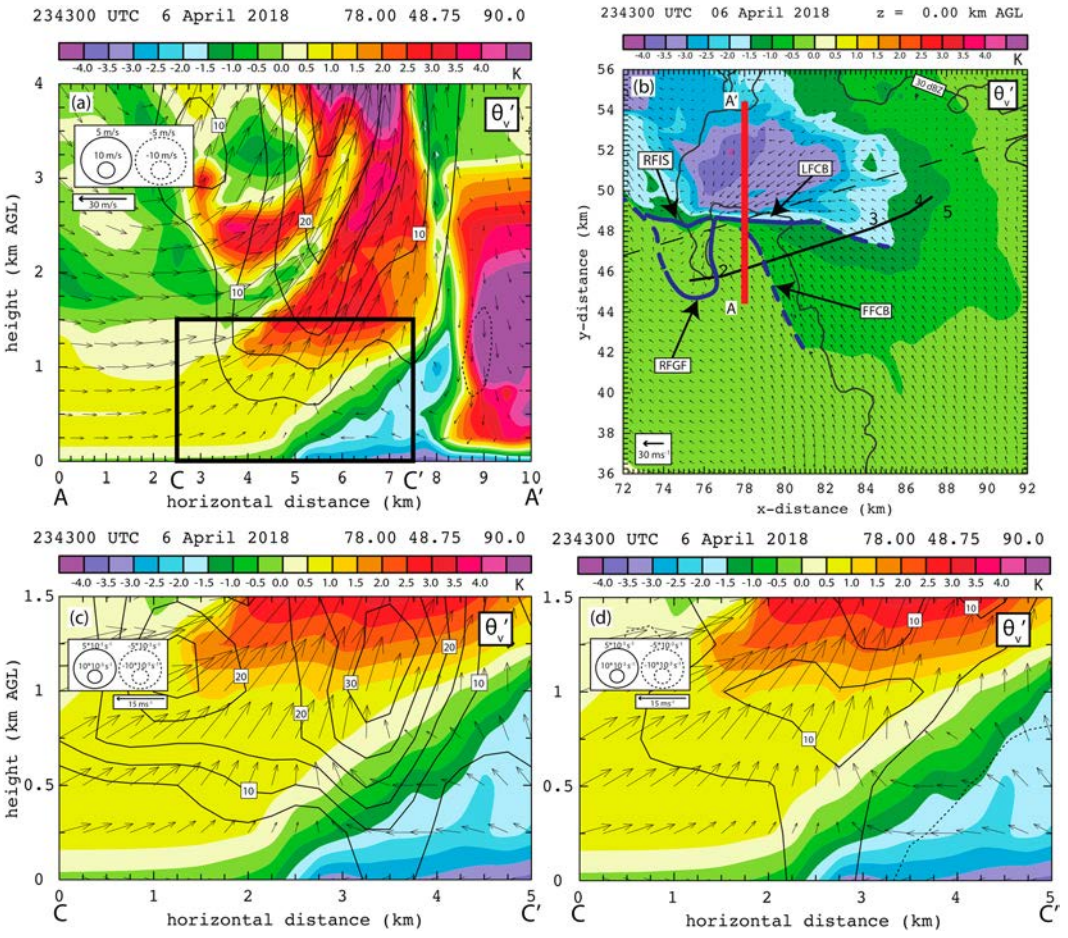

FIG. 9. Radar-analyzed and DLA-retrieved fields focused on the SVC at 2343 UTC. (a) South–north vertical cross section "A–A′" of color-filled θ_v' and contoured vertical velocity across the LFCB and SVC, located as in (b); (b) color-filled θ_v' with the 30-dBZ contour at the surface (as in Fig. 6c) with location of cross section "A–A′" in red; (c) zoomed vertical cross section "C–C′" of color-filled θ_v' and contoured streamwise vorticity in the subarea depicted by the box "C–C′" in (a); (d) as in (c), but with contoured vertical vorticity. Airflow vectors are storm relative.

increase in streamwise vorticity through 2343 UTC prior to entering the low-level updraft (Figs. 11a,b). The integrated sum of baroclinic (baroclinic solenoidal and hydrometeor loading) and barotropic (tilting and stretching) horizontal vorticity forcings along both representative trajectories demonstrate diverse growth mechanisms as these parcels approach and process through the SVC (Figs. 11c,d). Trajectory A, entering the SVC from the cool side of the LFCB, is characterized by a steady and significant baroclinic solenoidal development of streamwise vorticity along with barotropic development of streamwise vorticity of a similar magnitude prior to entering the updraft (Fig. 11c). In contrast, trajectory B features minimal baroclinic generation with predominant barotropic forcing of both streamwise and crosswise vorticity (Fig. 11d).

The integrated sum of baroclinically generated and barotropically generated streamwise vorticity show that the barotropic and baroclinic forcings play different roles for the two sets of trajectories within the SVC (Fig. 12). For most, but not all, SVC trajectories, there is some positive contribution of baroclinically generated streamwise vorticity by 2343 UTC (Fig. 12a). The eight trajectories with the greatest contributions of baroclinically generated streamwise vorticity—classified as the "baroclinic group"—correspond to the eight trajectories that originate on the cool side of the LFCB at 2337 UTC (Fig. 10b). The remaining six trajectories, classified as the "barotropic group," have lesser baroclinic streamwise generation, with some having minimal baroclinically generated streamwise vorticity. This grouping corresponds to the six trajectories which originate on the warm side of the LFCB at 2337 UTC in the modified southeasterly inflow (Fig. 10a). Most trajectories have a notable barotropic streamwise vorticity contribution leading up to and during their residence time in the SVC region prior to entering the updraft (Fig. 12b). Trajectory A, representing the baroclinic group, has marginally less positive streamwise barotropic tendency compared to the barotropic group represented by trajectory B, although there is not a distinct bifurcation in the amount of barotropically

generated streamwise vorticity between the baroclinic and barotropic groupings (Fig. 12b). The difference in barotropically generated streamwise vorticity between the two sets of trajectories is less than the difference in baroclinic generation between them.

e. Deep main updraft structure and evolution

The Monroe supercell's storm-scale deep main updraft underwent a gradual decline in maximum speed, volume, and mass flux during the 70-min analysis period (Fig. 13). This overall downward trend in updraft strength is punctuated by three distinct updraft pulses during the period of 2255–2307 UTC (0–12 min), 2315–2330 UTC (20–35 min), and again at 2340–2355 UTC (45–60 min), as further evidenced by a deepening of the 50+ dBZ maximum reflectivity (Figs. 13a–c). Although the magnitude and depth of the first pulse is much greater than the second and third, all pulses feature a local increase in magnitude and depth of updraft mass flux (Fig. 13c). Additionally, all three updraft pulses are associated with relatively intense low-level mesocyclones either just prior to or in the early stages of the pulse, including a potentially pretornadic circulation at 2315 UTC (e.g., as discussed in Hosek 2022), and the EF0 tornado–cyclone at 2343 UTC with the second and third pulse, respectively (Fig. 13d).

Storm-scale vertical cross-sections following and oriented with the storm motion are used to further investigate the updraft evolution from 2343 to 2352 UTC (Fig. 14). At 2343 UTC (Figs. 14a,c), the supercell updraft features a peak vertical velocity of 25 m s^{-1} at 2–5 km with a broad column of updraft exceeding 15 m s^{-1} extending to 7 km above the bounded weak echo region (BWER) (Fig. 14c, x = 3.5 km). A small column of 50 dBZ extending above 7 km at 2343 UTC is located above the strongest and deepest portion of the main updraft, indicating consistency between the reflectivity and radar-analyzed wind field (Fig. 14c, x = 3.5 km).

At 2352 UTC, the strongest portion of the updraft is east-northeast of the low-level updraft position and maximized in the upper levels (Figs. 14b,d). The supercell updraft features dual vertical velocity peaks of 25 m s^{-1} in the 6–8-km layer (Fig. 14d, x = 4 km) and to the northeast in the 7–9-km layer (Fig. 14d, x = 5 km). Both of these maxima are within a broad column of updraft exceeding 15 m s^{-1} extending in the 1–12-km layer above the BWER (Fig. 14d, x = 4.5 km). An extensive upward expansion of reflectivity is associated with this deepened updraft pulse, which appears to correspond to the low- to midlevel updraft pulse at 2343 UTC advected east-northeast along the storm motion vector as associated parcels rose (Fig. 14d, x = 5–7 km, height = 9–12 km). The top of the elevated updraft pulse and its associated reflectivity at 2352 UTC extends about 4 km higher than the storm top at 2343 UTC, equivalent to an average updraft-top rise rate of about 7.5 m s^{-1}. Although the SVC trajectories at 2343 UTC had risen to 8–10 km by 2352 UTC (not shown) and still have positive vertical velocity, there is insufficient evidence to hypothesize a causal relationship between the SVC and subsequent updraft deepening.

5. Discussion

a. Comparison of the radar-analyzed/retrieved LFCB and FFCB to modeled storm boundaries

The kinematic and thermodynamic properties of the present radar-analyzed and retrieved LFCB have several similarities to the simulated LFCBs identified by BW13 and S21. An equivalent potential temperature (θ_e) gradient is associated with the LFCBs in the aforementioned modeling studies, while only a minimal θ_e gradient exists across the simulated FFCBs. The present retrieved θ_e field at both 2343 and 2352 UTC similarly reveals a minimal θ_e gradient across the FFCB (~0.5 K km^{-1}) and a significant θ_e gradient of about 3 K km^{-1} across the LFCB (Fig. 15). Notably, the minimum θ_e perturbation in the Monroe supercell cold pool is significantly smaller than in the S21 cold pool (~−8 versus ~−20 K, respectively). The observed and modeled LFCBs are also delineated by significant θ_v gradients while the respective FFCBs have weak θ_v gradients. Additionally, both the presently observed and BW13-modeled LFCBs rotate counterclockwise toward the left-forward supercell flank during the course of cold pool evolution and have associated baroclinically generated streamwise vorticity. Following the convention that a line parallel to storm motion through the main updraft and low-level mesocyclone separates left and right flanks, the observed LFCB is actually about 25° to the right of storm motion at 2343 UTC (LFCB versus long dashed line in Figs. 6 and 15) and thus technically a "right-flank convergence boundary" at that time.[3] However, both the BW13 and S21 simulations are of traditional Northern Hemisphere midlatitude supercells with a forward-flank precipitation region that extends into the front-left flank (e.g., Fig. 1), whereas the forward anvil precipitation shield of the Southeast, cool-season Monroe supercell uniquely extends significantly southward despite the east-northeastward storm motion (e.g., Figs. 6–8). The southward-extending forward anvil precipitation shield of the Monroe supercell has thus effectively rotated the initial LFCB position clockwise (via the DLA's diabatic cooling, transportive, and frontogenetic forcings) relative to the simulated LFCBs (BW13; S21).

b. Process evolution of the Monroe supercell's SVC related to storm morphology

Regions of streamwise vorticity maxima are observed in the Monroe supercell throughout the analysis period. The streamwise vorticity maximum along the LFCB at 2343 UTC has a somewhat tube-like character extending to the low-level updraft (Fig. 6). This tube-like structure extends along the LFCB from the updraft at x = 77 km through x = 82 km (not shown). While simulations (Orf et al. 2017; S21) and observations of SVCs in High Plains (Murdzek et al. 2020; S21) and Great Plains supercells (S21) have shown SVCs to persist for

[3] The research community could improve the conventional terminology for the presently named FFCB and LFCB to allow for potential changes in quadrant (e.g., counterclockwise LFCB rotation) and differing initial quadrants associated with internal storm boundaries spanning all environments.

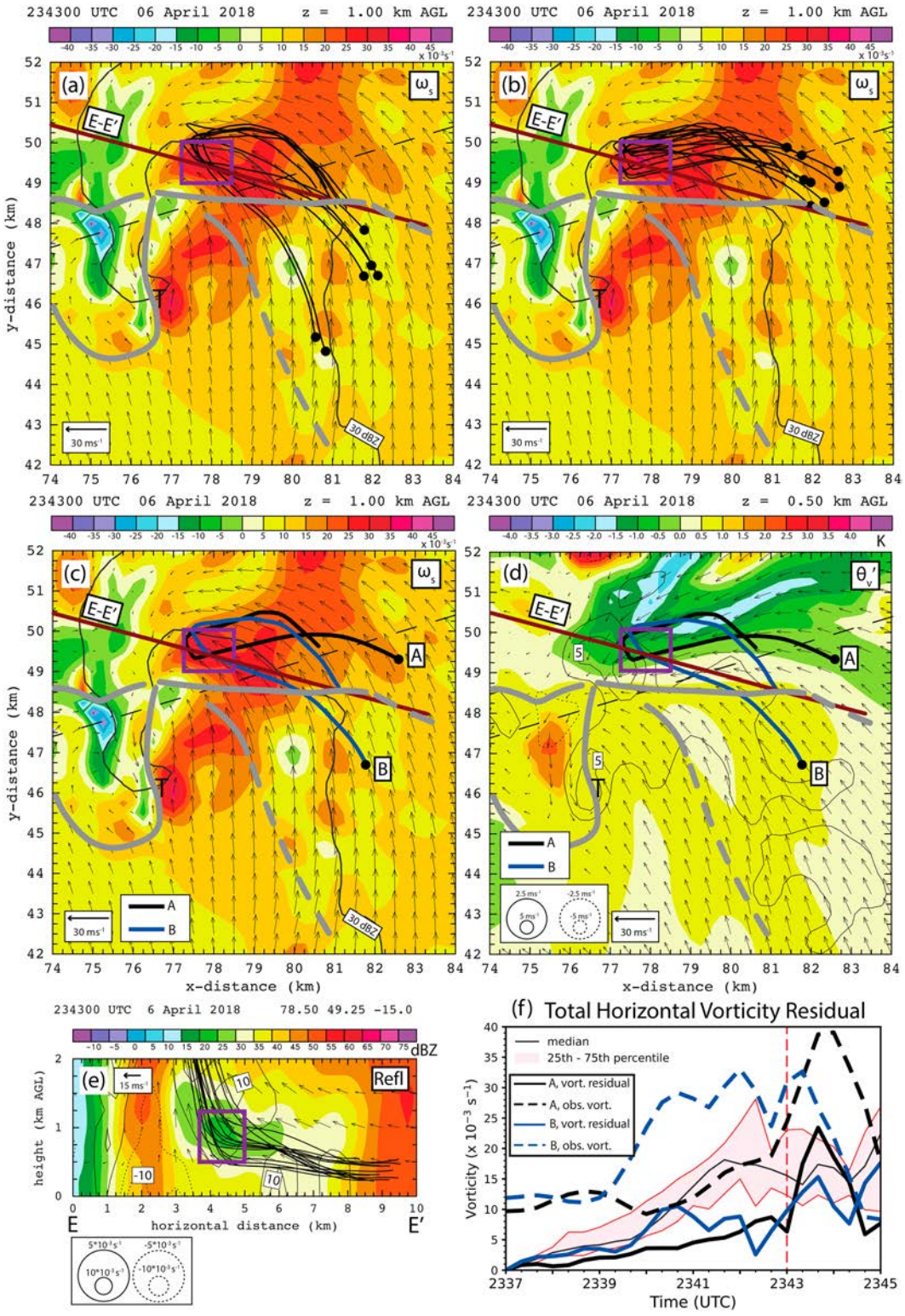

FIG. 10. Fourteen storm-relative DLA-derived air trajectories from 2337 to 2352 UTC, which pass through the SVC at 2343 UTC, referenced against radar-analyzed and DLA-retrieved fields at 2343 UTC. Storm internal boundaries are denoted by the gray lines in (a)–(d). (a) Horizontal projection of trajectories originating on the warm side of the LFCB overlaid on color-filled streamwise vorticity and 30-dBZ contour at 1 km. Black dots denote the parcel

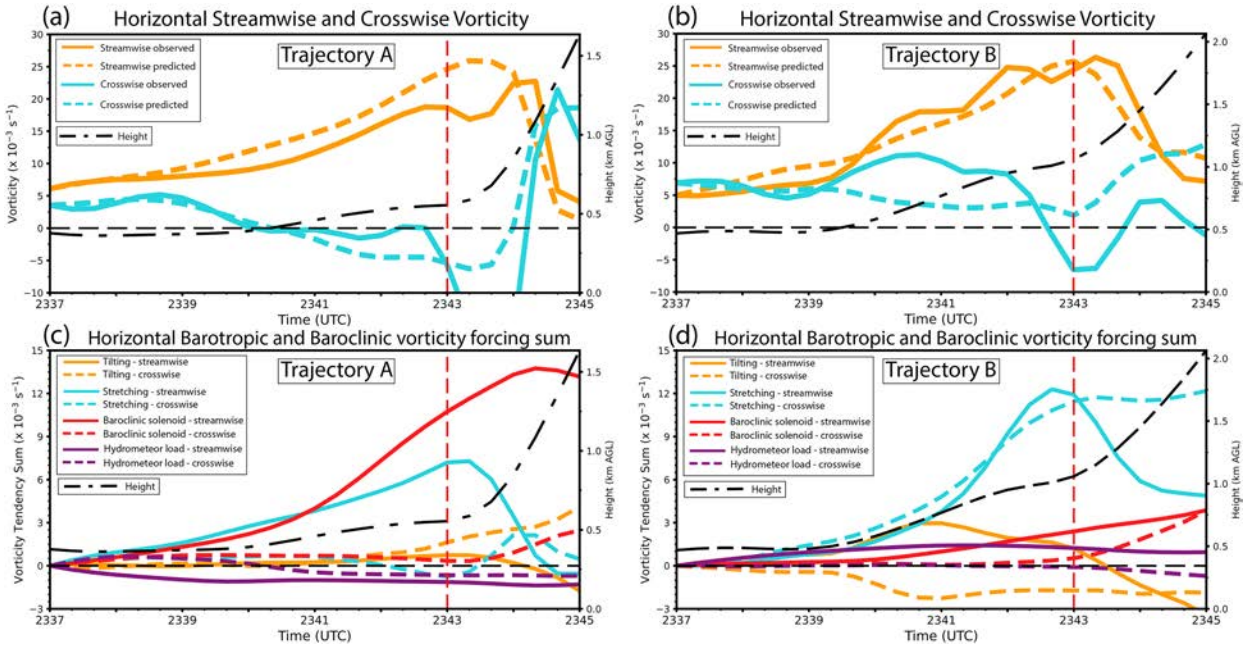

FIG. 11. Time series of observed and predicted horizontal vorticity and horizontal vorticity tendency terms during the period 2337–2345 UTC. Observed (solid) and predicted (dashed) streamwise and crosswise vorticity for representative trajectory (a) A and (b) B; and the integrated sum of baroclinic and barotropic horizontal vorticity tendencies for representative trajectory (c) A and (d) B. Parcel height is represented by the dash–dot black line associated with the right axis. The horizontal dashed black line denotes zero vorticity/vorticity tendency. The vertical red dashed line locates the 2343 UTC analysis time. Solid lines denote streamwise vorticity and dashed lines denote crosswise vorticity in (c) and (d).

about 30 min, the Monroe supercell's SVC is directly observed for about 10 min, and given the spacing between analyses could have persisted for upward of 20 min. The vortexgenesis mechanisms of the Monroe supercell's SVC are consistent with previously identified SVC origin and maintenance processes. It should be noted that some of the supercells which have been studied in this context are significantly stronger and longer-lived than the Monroe supercell [e.g., Orf et al. (2017), who simulate a long-lived EF5 tornado].

A well-defined radar-analyzed rotorlike circulation along the LFCB below 1.25 km is collocated with horizontal confluence, a mesoscale updraft, an intense and compact low-level streamwise vorticity maximum above the surface, and a well-defined DLA-retrieved baroclinic zone (Fig. 9). While there is some uncertainty in the trajectory vorticity retrieval owing to nontrivial residuals, the reasonably low residuals of the representative trajectories enable us to draw some broad conclusions regarding the character of trajectory groupings (Fig. 10f). Both the baroclinic solenoidal mechanism (due to the horizontal virtual density gradient) and the barotropic horizontal tilting and stretching process (due to acceleration toward the low-level updraft) contribute streamwise vorticity within the SVC, consistent with previous simulations (S21). However, the relative importance of the observed baroclinic and barotropic mechanisms differ depending on parcel source region. Parcels entering the SVC from the cold pool (left) flank of the LFCB have baroclinically generated streamwise vorticity on the same order of magnitude of, and potentially exceeding, barotropically generated streamwise vorticity (Fig. 11c). Meanwhile, parcels entering from the LFCB's inflow (right) flank along and east of the FFCB contain a dominant barotropic contribution with minimal baroclinically generated streamwise vorticity (Fig. 11d). This differs somewhat from the parcels of the S21 simulation, where parcels which were dominated by barotropic generation of horizontal vorticity were located further on the cool side of the baroclinic boundary than

←
location at 2337 UTC; (b) as in (a), but with trajectories originating on the cool side of the LFCB; (c) as in (a), but with only labeled representative trajectories A and B shown; (d) as in (c), but with trajectories overlaid on color-filled θ_v' with contoured vertical velocity at 0.5 km; (e) all 14 trajectories projected on vertical cross section "E–E′" [located in (a)–(d)] up to 2 km (roughly corresponding with parcel location at 2345 UTC) with color-filled reflectivity and contoured vertical vorticity; (f) time series of median (gray line) and 25th–75th percentile range (red shading) of horizontal vorticity residual magnitude through 2345 UTC for all trajectories, with the vertical red dashed line denoting the 2343 UTC analysis time. The horizontal vorticity residual magnitude of representative trajectory A (black, solid) and B (blue, solid) are shown, as well as their observed horizontal vorticity magnitude (A is black dashed; B is blue dashed). Airflow vectors are storm-relative. The "T" locates the tornado–cyclone.

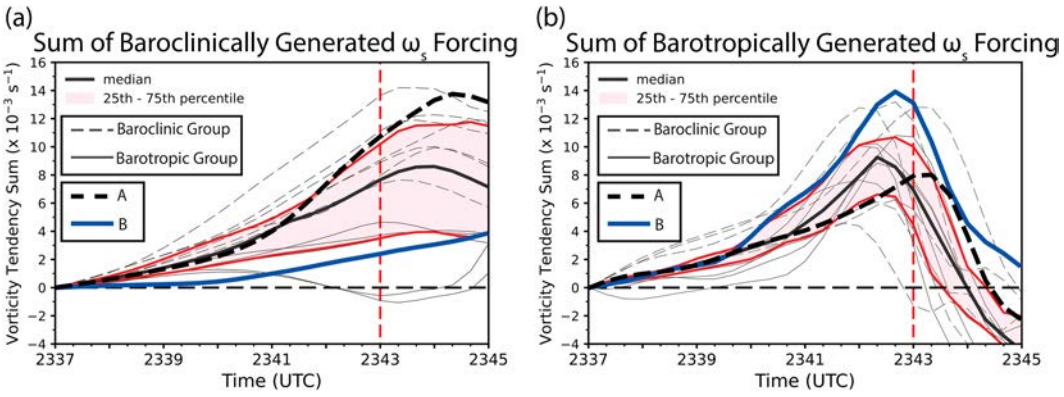

FIG. 12. Time series of baroclinic and barotropic production of streamwise vorticity during the period 2337–2345 UTC. Representative Trajectories A and B are denoted by the thick black-dashed and blue lines, respectively. All other trajectories are shown as thin gray lines, with solid lines representing the barotropic group and dashed lines representing the baroclinic group. (a) Integrated sum of baroclinically generated streamwise vorticity forcing, with the median (dark gray line) and 25th–75th percentile (red shading). (b) Integrated sum of barotropically generated streamwise vorticity median (dark gray line), 25th–75th percentile (red shading). The vertical red dashed line locates the 2343 UTC analysis time.

the parcels dominated by baroclinic generation. However, the structural differences between our observed supercell and the S21 simulated supercell, and resulting differences in trajectory source region, may be the source of this discrepancy. Additional observations of SVCs in supercells with a more similar environment and structure to the S21 simulated supercell will be needed to more directly compare with their simulation.

The observed SVC parallels the LFCB directly into the supercell updraft (Figs. 6a,b at $x = 77.25$ km, $y = 49.00$ km), where streamwise vorticity is subsequently tilted into vertical vorticity and stretched in the low-level updraft (not shown). While the intensification of the storm updraft and tornadogenesis just prior to 2343 UTC coincides with the development of an SVC, there is no direct evidence that the SVC is dynamically significant for either process. At 8 min prior to the updraft intensification and evidence of an SVC (i.e., at 2335 UTC), the local maximum of streamwise vorticity in the storm inflow is not attributable to a thermodynamic boundary internal to the storm (Fig. 5b). This initial inflow streamwise vorticity is consistent with recent simulations emphasizing the importance of parcels entering the mesocyclone from storm inflow (e.g., Coffer et al. 2023). It is hypothesized that this vorticity could have catalyzed initial storm intensification via an increase in midlevel updraft vertical vorticity, in turn causing a perturbation pressure reduction of order $\delta\pi' \sim -\delta(\zeta^2)$ followed by increased $\partial\pi'/\partial z$ that could accelerate the main updraft (Klemp and Rotunno 1983). The subsequent intensification of the low-level updraft could in turn result in accelerated low-level airflow toward the updraft, thereby aligning an easterly flow along the LFCB favorable for parcels to experience a long residence time in a zone favorable for baroclinic generation of streamwise vorticity and also further enhancing this vorticity via horizontal stretching. The established SVC could then feed enhanced streamwise vorticity to the low-level updraft for subsequent tilting and vertical stretching, either maintaining the intensified updraft or continuing the intensification process. In the Monroe supercell, the peak magnitude of streamwise vorticity in the SVC at 2352 UTC (45×10^{-3} s^{-1}), following the low-level mesocyclone peak intensification, is greater than at 2343 UTC (35×10^{-3} s^{-1}) (Figs. 6b and 8b). However, the rapid evolution of the supercell during this time, along with the 9-min gap between radar analyses, limits the ability to explain the dynamical origins of this magnitude increase.

This constructive feedback mechanism between the low-level updraft and SVC has been hypothesized in a recent simulation which featured coincident intensification of an SVC and low-level mesocyclone associated with imminent tornadogenesis (Finley et al. 2023). However, neither the Finley et al. (2023) simulation nor our observed case can categorically rule out alternative hypotheses that either: 1) the development of the SVC is the dominant catalyst to low-level mesocyclone intensification, or 2) the intensifying low-level mesocyclone and the associated increase in low-level horizontal stretching is the dominant catalyst to the development of the SVC, which itself is not a source of additional low-level mesocyclone intensification. It is also possible that the constructive feedback hypothesis or either of these alternate hypotheses may be more accurate for particular individual storms in different environments. Additional observational studies will be needed to achieve a more robust conclusion on this question.

None of the trajectories that traverse the SVC are either ingested into or wrapped around (i.e., as in Orf et al. 2017) the tornado–cyclone (Fig. 10). This result is consistent with recent observations that SVCs may not be an important mechanism for tornadogenesis in all supercells (Murdzek et al. 2020). Additionally, no link between SVC-generated vorticity and the RFD surge has been identified, the latter event we hypothesize may have had a role in tornadogenesis akin to previous observations (e.g., Lee et al. 2012; Kosiba et al. 2013; Marquis et al. 2012).

The Monroe supercell's SVC only develops as its cold pool begins to surge southward. The southward surge of the cold pool increases confluence along the LFCB and orients it such

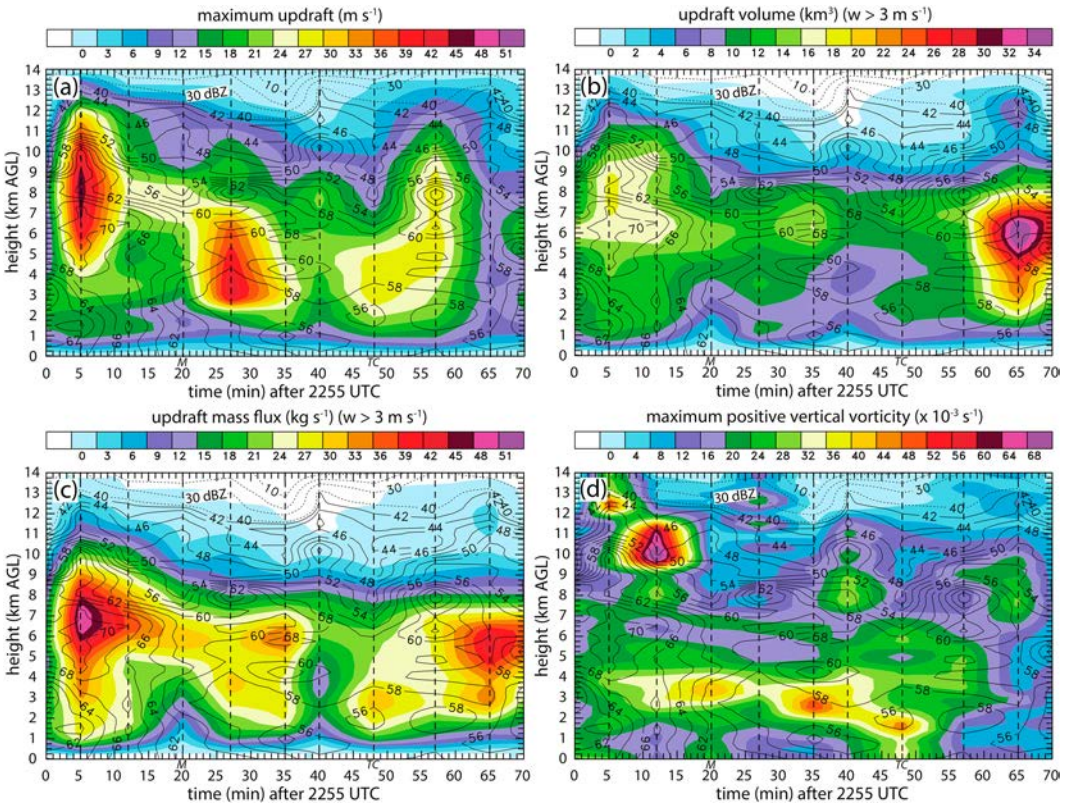

FIG. 13. Time series (in minutes after 2255 UTC) with height of maximum reflectivity (contoured) and (a) maximum updraft, (b) updraft volume for $w > 3$ m s^{-1}, (c) updraft mass flux for $w > 3$ m s^{-1}, and (d) maximum positive vertical vorticity. Time series were generated within a rectangular sampling volume centered on the storm updraft core region, dimensioned 10 km × 10 km horizontally and 14 km vertically, that moved with the storm and contained both the main northern updraft and the southern tornado–cyclonic updraft for the analysis duration. Radar analysis times are denoted by the vertical dashed lines. The time of the "early transient mesovortex" (Hosek 2022) and EF0 tornado–cyclone are designated on the time axis by "M" and "TC," respectively.

that parcels parallel it as they approach the main updraft. However, this surge also self-limits the SVC as continued southward movement undercuts the supercell updraft and reorients the LFCB counterclockwise close to 90° relative to the storm inflow. Consequently, the rotated LFCB is less conducive to long parcel residence times in the zone favorable for baroclinic generation and horizontal stretching of streamwise vorticity. Thus, the SVC in the Monroe supercell can be described as a short-lived transient feature.

The Monroe supercell's SVC also features multiple low-level vertical vorticity maxima of 10×10^{-3} s^{-1} leading into the low-level updraft (Fig. 7, $x = 77.5$, $y = 49.00$; and $x = 79.25$, $y = 48.75$). Although the temporal and spatial resolution of the present radar analysis is insufficient to directly compare this to the "parade of [vertical] vortices" seen in high-resolution simulations (e.g., Orf et al. 2017; S21), the broad expanse of positive vertical vorticity nevertheless differs notably from some previously observed SVCs which display no tendency for positive vertical vorticity (e.g., Murdzek et al. 2020). This could be due to differences in radar-observed velocity fields, analysis techniques, spatial resolution, or environmental conditions. A larger inventory of observed SVCs will be necessary to determine if the Monroe supercell's SVC would classify as "unusual" compared to other supercells.

c. *Comparison of the Monroe supercell to southeastern HSLC supercells*

The Monroe supercell's forward-flank surface cold pool θ'_v deficit from 2343 to 2352 UTC is as large as 4 K relative to the background environment (Figs. 6 and 8). This weak-moderate forward-flank cold pool is common in Southeast supercells, including nontornadic supercells (WP21). In the context of Great Plains supercells, it has been demonstrated that forward-flank cold pool deficits greater than −5 K are less likely to be associated with tornadic supercells (Markowski et al. 2012a,b; Shabbott and Markowski 2006). Air immediately behind the Monroe supercell's RFGF has θ_v within 0.5 K of the inflow in the vicinity of the tornado–cyclone, with the coldest FFD cold pool air remaining more than 2 km from the tornado–cyclonic inflow (Fig. 6). The minimal rear-flank cold pool intensities are generally consistent with Great Plains tornadic supercell RFDs, which feature θ'_v values only slightly lower than their inflows, in contrast to nontornadic supercell RFDs featuring a greater θ'_v deficit (Markowski et al. 2002;

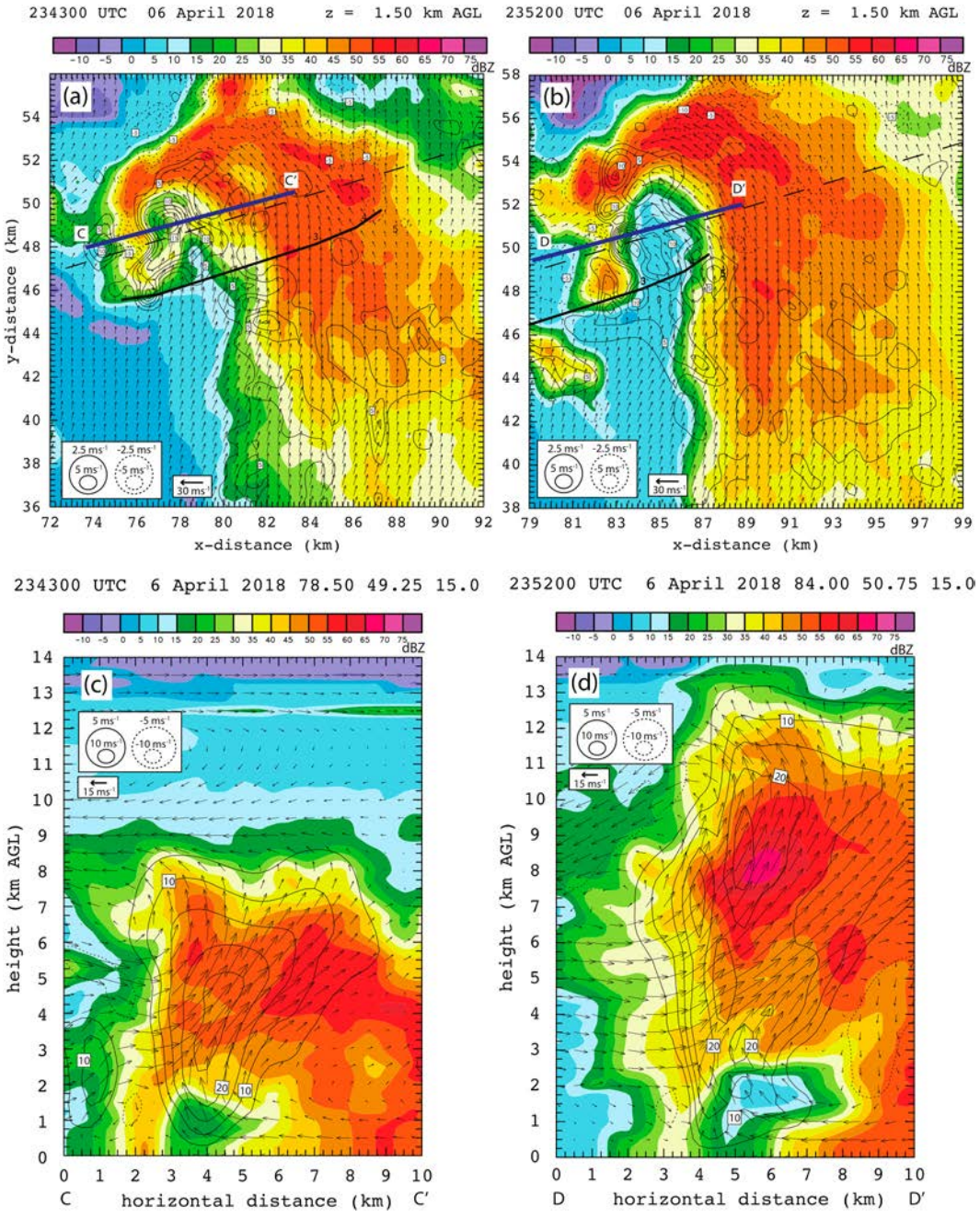

FIG. 14. Comparison of color-filled reflectivity and contoured vertical velocity in the Monroe supercell at 2343 and 2352 UTC. (a) Horizontal projection at 1.5 km and 2343 UTC; (b) as in (a), but at 2352 UTC; (c) vertical cross section C–C′ at 2343 UTC; (d) as in (c), but for cross section D–D′ at 2352 UTC. Cross-section locations are denoted by the labeled blue line in (a) and (b). Airflow vectors are storm relative.

Grzych et al. 2007; Hirth et al. 2008; Weiss et al. 2015; Markowski et al. 2012a). While the Monroe supercell's FFD and RFD cold pools are consistent with cold pools observed in Great Plains tornadic supercells, it remains unclear due to a lack of in situ observations if FFD or RFD cold pool intensity can usefully discriminate between tornadic and nontornadic supercells in the Southeast, given the other environmental and geographic differences in the region which might impact storm evolution and tornadogenesis.

The Monroe supercell evolves within a high-shear, moderate MLCAPE environment in contrast to an HSLC environment. Although the Monroe storm environment contains high shear, the roughly 1900 J kg^{-1} of MLCAPE (Fig. 3a) is nearly double that of typical HSLC environments (e.g., WP21). However, the

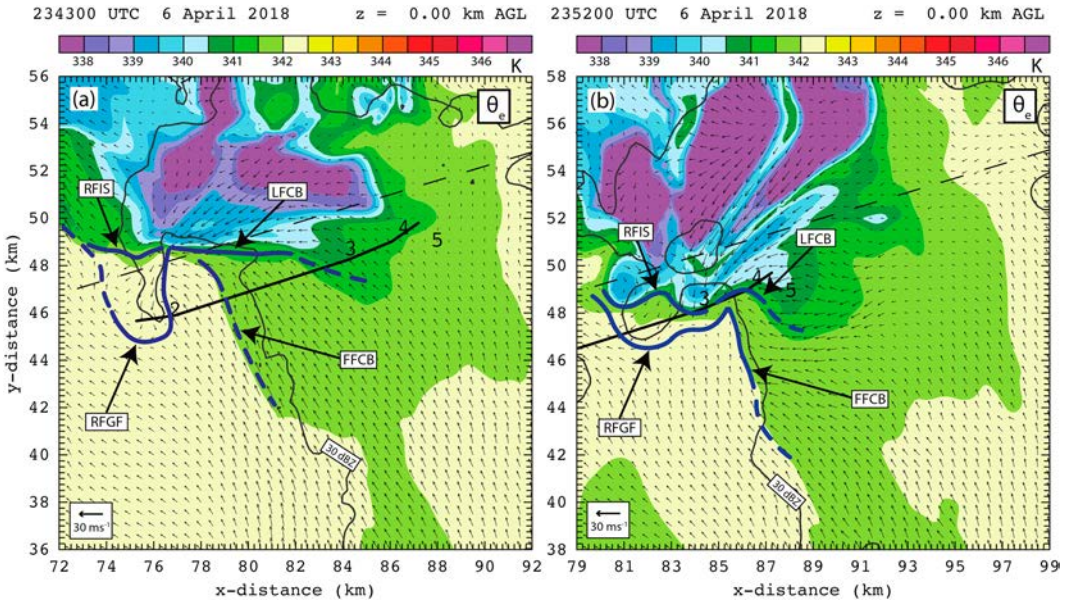

FIG. 15. Color-filled equivalent potential temperature (θ_e) with reflectivity contoured at 0 km at both (a) 2343 and (b) 2352 UTC. Surface boundaries are presented in blue and the surveyed tornado track is presented in black as in Fig. 6. The surface boundaries are labeled. Airflow vectors are storm-relative wind.

thermodynamic profile from the proximity sounding demonstrates an otherwise Southeast-like environment including a moist BL, shallow EML, and a moist mid and upper-level profile with relatively meager lapse rates compared to typical Great Plains environments (Figs. 3a,b).

The Monroe supercell's updraft at 2343 and 2352 UTC features a broad core region locally exceeding 10–15 m s^{-1} (Fig. 14). The maximum updraft of 25 m s^{-1} at 2343 UTC is located in the midlevels as opposed to the upper-levels in a high-CAPE storm, suggesting that dynamic pressure perturbation forces were the dominant source of vertical acceleration. This is consistent with HSLC simulations (WP21) and earlier Southeast supercell observations (Murphy and Knupp 2013). Three distinct updraft pulses which deepen the 50 dBZ reflectivity by 2–3 km are observed approximately 10 min apart during the analysis period (Fig. 13). With the exception of individual deep updraft pulses, the maximum updraft speeds tend to be in the range of 5–7 km (Fig. 13a), consistent with the low-CAPE simulations of WP21. The distinct deep updraft pulses resemble the "weak evolution" storm mode described by Foote and Frank (1983) that is also evident in simulated low-CAPE supercells (WP21). Despite the relatively large amount of environmental CAPE, the Monroe supercell's morphology and evolution share similarities to low-CAPE Southeastern supercells. This behavior is hypothesized to be caused by the weak temperature lapse rates throughout the vertical profile that are consistent with typical Southeast environments.

Trajectories ingested by the low-level tornado–cyclone at 2343 UTC originate from the precipitation-free storm inflow (Figs. 16a,b). These trajectories never go within ~2 km of the main supercell updraft and SVC at low levels (Figs. 10c,d versus Figs. 16a,b), and do not travel along the cool side of the weakly baroclinic FFCB. After entering the tornado–cyclonic updraft and accelerating sharply upward, parcels rise more slowly in the tilted updraft (Figs. 16c,d). The vertical velocity of some parcels briefly become vanishingly small around 2–3 km AGL, while the other trajectories maintain a steady vertical velocity. This behavior differs from typical high-CAPE storms, wherein parcels continue to accelerate toward the EL due to positive buoyancy exceeding the downward dynamical pressure perturbation force above an intense midlevel mesocyclone (WP21). Despite some similarities to the trajectories of low-CAPE simulations of WP21, the observed trajectories of the Monroe supercell maintain a positive vertical velocity through and above the midlevels. Although a pressure retrieval is beyond the scope of the present study, it is hypothesized that the larger updraft buoyancies available in the Monroe storm compared to the low-CAPE simulations of WP21 enable parcels to maintain positive vertical velocity despite being acted on by downward-directed perturbation pressure forces.

A previously undocumented morphological feature of southeastern cool season supercells is the shallow layer of weak baroclinity in the inflow region around 250–500 m (Figs. 6, 9, 10, and 16) that results from vertical transport of the superadiabatic lower convective BL by weak inflow-sector mesoscale updrafts (e.g., Ziegler et al. 1997). This superadiabatic layer lifting warms the mid-BL inflow compared to the forward anvil precipitation region. This feature is indicated by the warm θ'_v (+0.5 K) in the precipitation-free inflow sector bounded by the FFCB, LFCB, and RFGF across all shown analysis times (Figs. 5d, 6d, 8d, 9c,d, 10d, and 16b). While outside the scope of the present study, this interesting result bears further exploration in a future study.

6. Conclusions

This paper presents the first study to the authors' knowledge featuring time-dependent, 3D multiradar analyses and

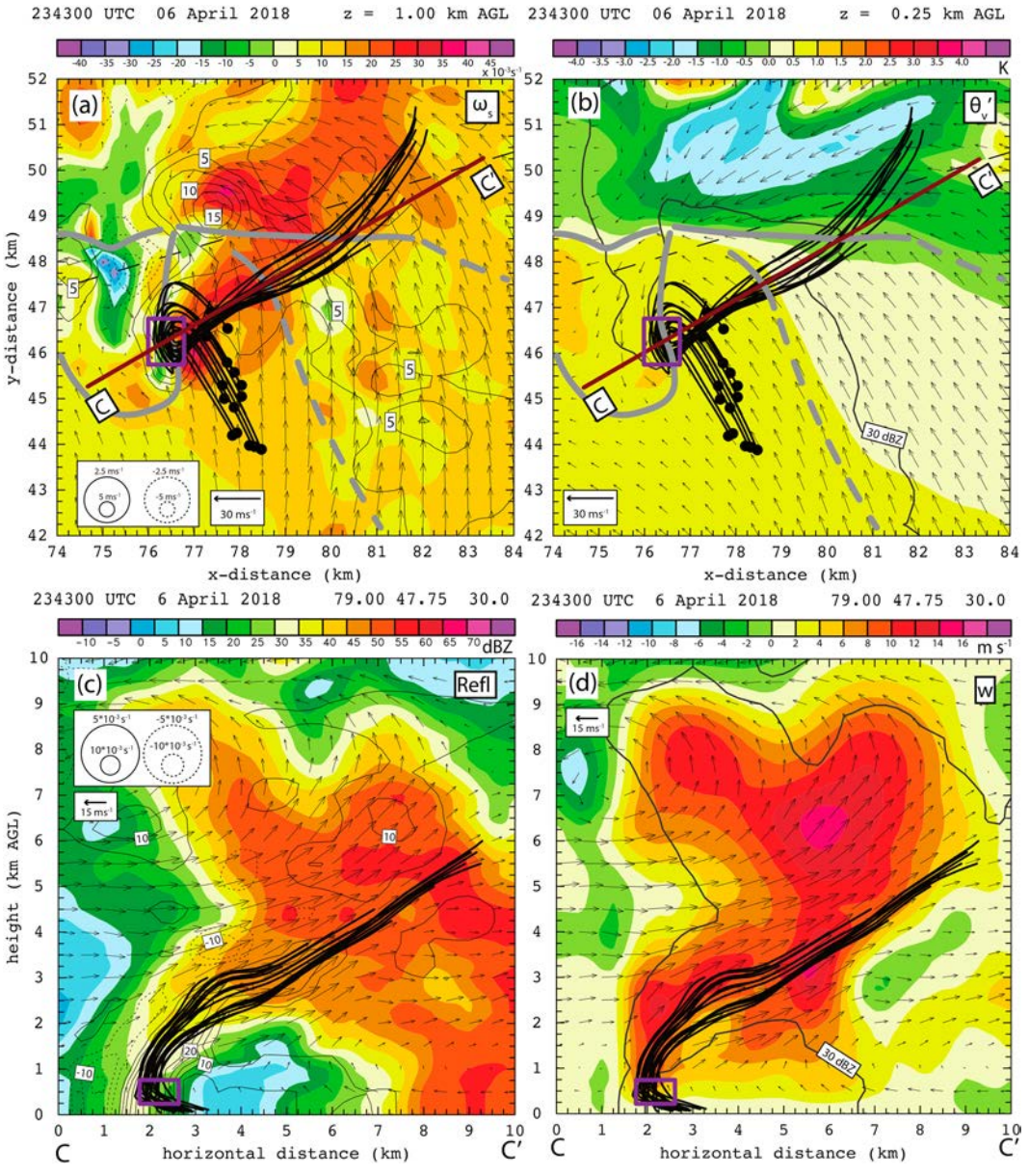

FIG. 16. Sixteen storm-relative DLA-derived air trajectories from 2335 to 2352 UTC, which passed through the low-level tornado-cyclone at 2343 UTC, denoted by the purple box, referenced against radar-analyzed and DLA-retrieved fields at 2343 UTC. Gray lines denote the storm internal boundaries in (a) and (b). (a) Horizontal projection of trajectories overlaid on color-filled streamwise vorticity with contoured vertical velocity at 1 km; (b) trajectories overlaid on color-filled θ_v' with contoured 30-dBZ reflectivity at 0.25 km; (c) trajectories projected on vertical cross section C–C′ [located in (a)] and overlaid on color-filled reflectivity and contoured vertical vorticity; (d) as in (c), but with color-filled vertical velocity and contoured 30-dBZ reflectivity. Black dots in (a) and (b) denote parcel location at 2337 UTC. Airflow vectors are storm relative.

diabatic Lagrangian analysis (DLA) thermodynamic retrievals of a tornadic supercell in the Southeast United States. An array of four radars—two ground-based and two airborne—have sampled the 6–7 April 2018 Monroe supercell during the VORTEX-SE project at close range for over 1 h. Research soundings and unique CRL profiles obtained in coordination with the project have been used to initialize the DLA and enable a 4-D kinematic and thermodynamic analysis of the supercell. To the authors' knowledge, the resulting demonstration of internal consistency between the radar-analyzed kinematic and computed vorticity–dynamical fields utilizing the retrieved thermodynamic fields represents a unique finding.

A transient SVC has been identified as a tube-like volume of maximum streamwise vorticity along the LFCB. The associated density gradient is oriented roughly normal to the low-level flow toward the main supercell updraft, and a radar-analyzed

rotor circulation is collocated with this gradient. Due to the southward surge of the cold pool, the SVC is only evident for 10–20 min. However, parcels traversing the SVC accumulate large quantities of streamwise vorticity and enter the low-level updraft. About half of all parcels within the SVC experience significant baroclinic solenoidal generation of streamwise vorticity of a similar magnitude to their barotropic streamwise vorticity generation/enhancement. The other half of SVC trajectories primarily developed streamwise vorticity via barotropic processes. Although the development of the SVC is coincident with both the intensification of the supercell's mesocyclone and tornadogenesis, trajectory analysis demonstrates that parcels traversing through the SVC neither enter nor wrap around the tornado–cyclone. There does not appear to be a direct causal link between the development of the SVC and tornadogenesis; however, an indirect role via some unidentified nonlinear storm evolution process could not be ruled out.

This study also presents a uniquely high-resolution, 4D analysis of a supercell during the Southeast U.S. cool season. Despite a mesoscale environment featuring double the MLCAPE typically associated with HSLC environments, the Monroe supercell exhibits characteristics similar to the rather few HSLC supercell simulations and observations in the Southeast (e.g., WP21; Murphy and Knupp 2013). The Monroe supercell features a pulse-like updraft morphology distinct from typical conceptualizations of unicellular, quasi-steady supercells, while also remaining distinct from a typical multicell thunderstorm. The Monroe supercell's modest updraft achieves peak vertical velocity in the low- to midlevels rather than the upper-levels as in a typical high-CAPE storm, which importantly collocates large tilting and stretching tendencies with strong vertical shear of the horizontal wind. The inconsistencies between the Monroe supercell and typical HSLC supercells may be attributable to the greater MLCAPE present in this case. Studies of additional southeastern supercells in both HSLC and non-HSLC environments are needed to determine whether the HSLC-like structure of the Monroe supercell is the result of common thermodynamic profile structures in Southeast severe events (e.g., weak temperature lapse rates, etc.), or else if the Monroe supercell represents a case of a storm developing in a fringe HSLC environment. The analyses and methods presented herein will be used to investigate the origins of low-level rotation in the Monroe supercell's tornado–cyclone in a follow-on study.

Acknowledgments. Coauthors MIB (University of Oklahoma) and TAM (University of Louisiana, Monroe) led the collection of the C-band SMART-Radar and S-band KULM radar data, respectively. Coauthor ZW (University of Colorado, Boulder) led the operation of the CRL and provided its postprocessed data. Dr. Dan Stechman is gratefully acknowledged for assisting with application of the radar editing script and radar analysis codes, while Todd Murphy and Gordon Carrie are thanked for providing access to the KULM and SMART-Radar data, respectively. The authors gratefully acknowledge the staff of the NOAA Aircraft Operations Center (AOC) for their capable and dedicated operation of a P-3 Hurricane Hunter aircraft in support of VORTEX-SE (2018). The authors also gratefully acknowledge the many additional project participants who assisted with the utilized data collections. The third coauthor (MIB) and Dr. Cameron Homeyer (University of Oklahoma) are thanked for serving on the lead author's master's thesis committee, along with the first coauthor (CLZ) who served as the lead author's thesis research advisor, providing helpful collective feedback on this study. Comments offered by three anonymous formal reviewers helped to greatly improve the manuscript. The authors would also like to thank Alex Schueth (Texas Tech University) for his insightful, detailed comments regarding the classification of internal storm boundaries. This work was partially supported by National Science Foundation Award AGS-1917701. Coauthor MIB's role in this work was supported by NOAA Research Award NA160AR4320115. Coauthor TAM's role was supported by NOAA Research Award RA133R18SE0299. Coauthor ZW's role was supported by National Science Foundation Award AGS-1917693. Computing, infrastructure, and VORTEX-SE travel support were provided by the National Severe Storms Laboratory.

Data availability statement. Radiosonde data from the University of Louisiana–Monroe, flight-level in-situ data from the NOAA P-3, and radar data from the NOAA P-3 (TDRs), the University of Oklahoma School of Meteorology (dual SRs), and the University of Louisiana–Monroe (KULM) are available online from the VORTEX-SE (2018) EOL data catalog via the URL "https://data.eol.ucar.edu/master_lists/generated/vortex-se_2018/." Data from the Compact Raman Lidar (CRL) are available from University of Colorado Boulder CU Scholar (https://doi.org/10.25810/G7V9-NB56). Surface station observations can be found at NOAA National Center of Environmental Information Climate Data (https://www.ncdc.noaa.gov/cdo-web/datasets#LCD).

APPENDIX A

Diabatic Lagrangian Analysis

The diabatic Lagrangian analysis (Ziegler 2013a,b; DiGangi et al. 2016) manages the linear interpolation of airflow, reflectivity, vertical vorticity, and a recently introduced eddy mixing coefficient based on the 3D airflow deformation (Brandes 1984; Schlesinger 1978) in time and space from the merged-domain radar analyses to Lagrangian points following each trajectory. An updated version of the original DLA mixing term [i.e., Eq. (22) of Ziegler (2013a)] take the revised form

$$D_{\phi} = -[K_{\phi}(\pi/L_d)^2][\phi(x, y, z, t) - \phi_B(x, y, z)], \qquad \text{(A1)}$$

where the scalar fields θ and q_v are denoted by ϕ, $\phi_B(x, y, z)$ is the base state field, the scalar difference (Ziegler 2013a) is now assumed to be a half-sinusoid maximum, and K_{ϕ} ($m^2\ s^{-1}$) is the scalar eddy mixing coefficient assuming turbulent Prandtl Number Pr = 3.0. The mixing length L_d (m) is expressed as

$$L_d = \max[L_0 - 10^3(|\zeta| - \zeta_0)\Delta L_{\zeta},\ L_{\min}] \quad (|\zeta| - \zeta_0 \geq 0), \qquad \text{(A2)}$$

where ζ is vertical vorticity (s^{-1}), $\zeta_0 = 5 \times 10^{-3}$ (s^{-1}), $\Delta L_\zeta = 50$ m $(10^3\ s^{-1})^{-1}$, $L_0 = 3000$ m, $L_{min} = 300$ m, and other variables are defined in the text. The base mixing length L_0 broadly spans the depth of the cold pool and the width of main horizontal thermal gradients in the storm. The locally enhanced mesoscale mixing via the vorticity-dependent decrease of mixing length crudely parameterizes impacts of (presumably incompletely resolved) intense vertical motions on the edges of strong localized mesovortices, such as observed by Atkins et al. (2012) and Kosiba et al. (2013), that may enhance both the vertical redistribution of dynamically entrained environmental air and local parcel mixing (Markowski et al. 2012a).

Backward 3D trajectories spanning the merged radar analysis domain (see sections 2c,d, Fig. 2, and Table 3) are computed with a 20-s time step for up to 2 h from all grid points within the DLA domain back into their remote radar-analyzed inflow environments. Additional "pseudo-analyses" are generated by advecting the 2255 UTC merged-domain radar analysis backward in time with the storm motion with interpolation to the fixed merged grid domain to help backward air trajectories access their inflow environments. The back-advected pseudoanalyses are generated in the period 2155–2250 UTC at a 5-min interval to ensure that all trajectories after passing from the storm into the weakly heterogeneous inflow environment can subsequently reach either the homogenous remote environment or the radar analysis domain edge to be initialized. Note that all backward trajectories have previously exited the Monroe storm well after its 2220 UTC initiation time prior to entering the near-inflow environment. All trajectories found to originate within the convection-free inflow environment (i.e., about 99% of all initialized trajectories) are then assigned the θ, q_v, and pressure values of an environmental parcel interpolated to the initial Lagrangian height from the composite sounding formed by merging the CRL profile with the 2234 UTC Gilbert, Louisiana, sounding (section 3). Following the prescription of initial trajectory thermodynamics, the ordinary differential heat and water substance continuity equations are integrated forward in time along the individual backward trajectory paths. Using airflow and reflectivity, calculations using bulk parameterized microphysical terms diagnose snow, graupel/hail, and rain mixing ratios and compute parameterized rates of condensation/evaporation, collection/riming, freezing/melting, and deposition/sublimation at every Lagrangian point along each trajectory. Forward integration of all trajectories back to their originating gridpoint followed by a gather operation yields the 3D thermodynamic fields at each analysis time (Ziegler 2013a,b). Any very rare missing grid points resulting from noninitialization are hole-filled, followed by optional low-pass filtering of the predicted variables to suppress any variability over one grid interval due to possible decorrelation of adjacent trajectories.

APPENDIX B

Compact Raman Lidar

Analysis of the profiled air temperature and water vapor mixing ratio (q_v) from the downward-pointing compact Raman lidar (CRL) system (Liu et al. 2014; Wang et al. 2016) has employed the lidar scattering ratio or LSR (i.e., ratio of total return power to molecular return power) to determine regions where weak signal returns provide unreliable thermodynamic measurements due to cloud or precipitation attenuation. For the present study, LSR values exceeding 2 are used to identify signal attenuation by intervening cloud or precipitation. Weaker lidar signals caused by the P-3's optical window contamination during the 2018 CRL deployment have likely somewhat increased random error levels compared with nominal CRL measurements (Wu et al. 2016). In addition, temperature data in the first 200 m below the P-3 and water vapor mixing ratio (q_v) in the first 100 m below the P-3 are also masked due to large uncertainties associated with different overlap functions among two lidar channels in close proximity to the CRL.

Additional thermodynamic variables including potential temperature (θ), virtual temperature (T_v) and potential temperature (θ_v), dewpoint temperature, and relative humidity (RH) are derived from the Bolton (1980) formulas. Vertical pressure levels for these calculations are obtained using a downward integration of CRL-derived T_v via the hypsometric equation initialized with flight-level measured pressure and T_v. These derivations reveal small subregions with RH in excess of 100% (at times exceeding 130%). It is hypothesized that these infrequent nonphysical supersaturations are caused by either low-biased temperature or high-biased q_v. A mask is applied to gates suspected of containing low-biased temperature errors via an RH threshold varying nonlinearly from 90% at 0–100 m to 100% at 1 km MSL, thus removing approximately 10% of all gates. Exploring causes of these nonphysical RH values are outside the scope of the present study. The remote P-3 flight path locations preclude validation of the CRL profiles against (nonexistent) nearby fixed soundings or surface stations. Gaps in the data within a leg caused by the masking of regions with locally higher LSR or supersaturations are hole-filled via spatial piecewise horizontal linear interpolation.

APPENDIX C

Vector Vorticity Trajectory Calculations

Vorticity budgets are computed in the Cartesian (x, y, z) space of the radar analysis and DLA grid, followed by interpolation to Lagrangian points where the forcing terms are integrated in each time step, and finally conversion of the vector horizontal vorticity and individual forcing term components from Cartesian to natural coordinates at the Lagrangian point. The utilized conservation equations of the orthogonal (x, y, z) vorticity components (ξ, η, ζ) take the following form (e.g., Brandes 1983, 1984):

$$\frac{d\xi}{dt} = \left(\frac{\partial v}{\partial x}\frac{\partial u}{\partial z} - \frac{\partial w}{\partial x}\frac{\partial u}{\partial y}\right) - \xi\left(\frac{\partial v}{\partial y} + \frac{\partial w}{\partial z}\right) + \left(\frac{g}{\theta_{v0}}\frac{\partial \theta_v}{\partial y}\right) - \left(g\frac{\partial q_{hyd}}{\partial y}\right) + \left(f\frac{\partial u}{\partial z}\right) + \left(\frac{\partial F_z}{\partial y} - \frac{\partial F_y}{\partial z}\right), \quad \text{(C1)}$$

$$\frac{d\eta}{dt} = \left(\frac{\partial w}{\partial y}\frac{\partial v}{\partial x} - \frac{\partial u}{\partial y}\frac{\partial w}{\partial z}\right) - \eta\left(\frac{\partial u}{\partial x} + \frac{\partial w}{\partial z}\right) - \left(\frac{g}{\theta_{v0}}\frac{\partial \theta_v}{\partial x}\right) + \left(g\frac{\partial q_{\text{hyd}}}{\partial x}\right) + \left(f\frac{\partial v}{\partial z}\right) + \left(\frac{\partial F_x}{\partial z} - \frac{\partial F_z}{\partial x}\right), \tag{C2}$$

$$\frac{d\zeta}{dt} = \left(\frac{\partial w}{\partial y}\frac{\partial u}{\partial z} - \frac{\partial w}{\partial x}\frac{\partial v}{\partial z}\right) - \left[(\zeta + f)\left(\frac{\partial u}{\partial x} + \frac{\partial v}{\partial y}\right)\right] + \left(\frac{\partial F_y}{\partial x} - \frac{\partial F_x}{\partial y}\right), \tag{C3}$$

where θ_v is the DLA-retrieved virtual potential temperature (K), $\theta_{v0}(z)$ is the base-state virtual potential temperature (K), $g = 9.8\ \text{m s}^{-2}$ is the gravitational acceleration, $q_{\text{hyd}} = q_c + q_r + q_g + q_s + q_i$ is the total hydrometeor mixing ratio (kg kg^{-1}) from the DLA, $f = 10^{-4}\ \text{s}^{-1}$ is the Coriolis parameter, $\mathbf{F} = F_x\hat{\mathbf{i}} + F_y\hat{\mathbf{j}} + F_z\hat{\mathbf{k}}$ is the friction vector (Brandes 1984), and other variables are defined in the text. The first and second right-hand side (RHS) terms in Eqs. (C1)–(C3) represent tilting and stretching forcing, respectively, while the third through fifth RHS terms in Eqs. (C1) and (C2) are the thermal solenoid expressed in θ_v gradient form (e.g., Brandes 1984; Markowski and Richardson 2010; Ziegler 2013a), hydrometeor loading, and Coriolis forcing, respectively. The last RHS terms in Eqs. (C1)–(C3) are the turbulent forcing, approximated in the present calculations by $K_m\nabla^2\xi$, $K_m\nabla^2\eta$, and $K_m\nabla^2\zeta$, respectively, as suggested by Brandes (1983, 10–11), where the momentum eddy mixing coefficient $K_m = K_\phi/\text{Pr}$ (Pr = 3.0; see appendix A). A term proportional to the horizontal gradients of the perturbation Exner function π' is negligible at radar-resolved motion scales (Brandes 1983) and has been omitted from Eqs. (C1)–(C3).

Following integration of Eqs. (C1) and (C2) in each time step, the vector horizontal vorticity and its individual forcing term values in Eqs. (C1) and (C2) have been converted into their streamwise and crosswise components according to the direction of the storm-relative horizontal wind at Lagrangian points (Davies-Jones 1984). After subsequently calculating horizontal vorticity exchange terms between the streamwise and crosswise component directions (i.e., that conserve the horizontal vector vorticity magnitude) following the form of the last RHS terms in equations (9) and (10) of Roberts et al. (2016), the predicted streamwise and crosswise vorticity components are updated in the time step via their respective exchange terms.

REFERENCES

Adlerman, E. J., K. K. Droegemeier, and R. Davies-Jones, 1999: A numerical simulation of cyclic mesocyclogenesis. *J. Atmos. Sci.*, **56**, 2045–2069, https://doi.org/10.1175/1520-0469(1999)056<2045:ANSOCM>2.0.CO;2.

Alford, A. A., M. I. Biggerstaff, C. L. Ziegler, D. P. Jorgensen, and G. D. Carrie, 2022: A method for correcting staggered pulse repetition time (PRT) and dual pulse repetition frequency (PRF) processor errors in research radar datasets. *J. Atmos. Oceanic Technol.*, **39**, 1763–1780, https://doi.org/10.1175/JTECH-D-21-0176.1.

Anderson-Frey, A. K., Y. P. Richardson, A. R. Dean, R. L. Thompson, and B. T. Smith, 2019: Characteristics of tornado events and warnings in the southeastern United States. *Wea. Forecasting*, **34**, 1017–1034, https://doi.org/10.1175/WAF-D-18-0211.1.

Ashley, W. S., 2007: Spatial and temporal analysis of tornado fatalities in the United States: 1880–2005. *Wea. Forecasting*, **22**, 1214–1228, https://doi.org/10.1175/2007WAF2007004.1.

Atkins, N. T., A. McGee, R. Ducharme, R. M. Wakimoto, and J. Wurman, 2012: The LaGrange tornado during VORTEX2. Part II: Photogrammetric analysis of the tornado combined with dual-Doppler radar data. *Mon. Wea. Rev.*, **140**, 2939–2958, https://doi.org/10.1175/MWR-D-11-00285.1.

Barnes, S. L., 1964: A technique for maximizing details in numerical weather map analysis. *J. Appl. Meteor.*, **3**, 396–409, https://doi.org/10.1175/1520-0450(1964)003<0396:ATFMDI>2.0.CO;2.

——, 1970: Some aspects of a severe, right-moving thunderstorm deduced from mesonetwork rawinsonde observations. *J. Atmos. Sci.*, **27**, 634–648, https://doi.org/10.1175/1520-0469(1970)027<0634:SAOASR>2.0.CO;2.

Bartos, E. A., P. M. Markowski, and Y. P. Richardson, 2022: Three-dimensional thermodynamic observations in supercell thunderstorms from swarms of balloon-borne sondes. *Mon. Wea. Rev.*, **150**, 1689–1723, https://doi.org/10.1175/MWR-D-21-0122.1.

Beck, J., and C. Weiss, 2013: An assessment of low-level baroclinity and vorticity within a simulated supercell. *Mon. Wea. Rev.*, **141**, 649–669, https://doi.org/10.1175/MWR-D-11-00115.1.

Betten, D. P., M. I. Biggerstaff, and C. L. Ziegler, 2018: Three-dimensional storm structure and low-level boundaries at different stages of cyclic mesocyclone evolution in a high-precipitation tornadic supercell. *Adv. Meteor.*, **2018**, 9432670, https://doi.org/10.1155/2018/9432670.

Biggerstaff, M. I., and G. D. Carrie, 2019: SMART-R mobile radar data, version 1.0. UCAR/NCAR–Earth Observing Laboratory, accessed 1 November 2022, https://doi.org/10.26023/ZG88-YFBP-B50C.

——, A. A. Alford, G. D. Carrie, and J. A. Stevenson, 2021: Hurricane Florence (2018): Long duration single- and dual-Doppler observations and wind retrievals during landfall. *Geosci. Data J.*, **9**, 273–287, https://doi.org/10.1002/gdj3.137.

Bolton, D., 1980: The computation of equivalent potential temperature. *Mon. Wea. Rev.*, **108**, 1046–1053, https://doi.org/10.1175/1520-0493(1980)108<1046:TCOEPT>2.0.CO;2.

Brandes, E. A., 1983: Relationships between thunderstorm mesoscale circulation and tornadogenesis. Ph.D. dissertation, University of Oklahoma, 185 pp.

——, 1984: Relationships between radar-derived thermodynamic variables and tornadogenesis. *Mon. Wea. Rev.*, **112**, 1033–1052, https://doi.org/10.1175/1520-0493(1984)112<1033:RBRDTV>2.0.CO;2.

Chmielewski, V. C., D. R. MacGorman, C. L. Ziegler, E. DiGangi, D. Betten, and M. Biggerstaff, 2020: Microphysical and transportive contributions to normal and anomalous polarity subregions in the 29–30 May 2012 Kingfisher storm. *J. Geophys. Res. Atmos.*, **125**, e2020JD032384, https://doi.org/10.1029/2020JD032384.

Coffer, B. E., M. D. Parker, J. M. Peters, and A. R. Wade, 2023: Supercell low-level mesocyclones: Origins of inflow and vorticity. *Mon. Wea. Rev.*, **151**, 2205–2232, https://doi.org/10.1175/MWR-D-22-0269.1.

Cohen, R. A., and D. M. Schultz, 2005: Contraction rate and its relationship to frontogenesis, the Lyapunov exponent, fluid

trapping, and airstream boundaries. *Mon. Wea. Rev.*, **133**, 1353–1369, https://doi.org/10.1175/MWR2922.1.

Dahl, J. M. L., 2015: Near-ground rotation in simulated supercells: On the robustness of the baroclinic mechanism. *Mon. Wea. Rev.*, **143**, 4929–4942, https://doi.org/10.1175/MWR-D-15-0115.1.

——, M. D. Parker, and L. J. Wicker, 2014: Imported and storm-generated near-ground vertical vorticity in a simulated supercell. *J. Atmos. Sci.*, **71**, 3027–3051, https://doi.org/10.1175/JAS-D-13-0123.1.

Davies-Jones, R. P., 1982: Observational and theoretical aspects of tornadogenesis. *Intense Atmospheric Vortices*, L. Bengtsson and J. Lighthill, Eds., Springer, 175–189, https://doi.org/10.1007/978-3-642-81866-0_14.

——, 1984: Streamwise vorticity: The origin of updraft rotation in supercell storms. *J. Atmos. Sci.*, **41**, 2991–3006, https://doi.org/10.1175/1520-0469(1984)041<2991:SVTOOU>2.0.CO;2.

——, 2000: A Lagrangian model for baroclinic genesis of mesoscale vortices. Part I: Theory. *J. Atmos. Sci.*, **57**, 715–736, https://doi.org/10.1175/1520-0469(2000)057<0715:ALMFBG>2.0.CO;2.

——, and H. Brooks, 1993: Mesocyclogenesis from a theoretical perspective. *The Tornado: Its Structure, Dynamics, Prediction, and Hazards*, *Geophys. Monogr.*, Vol. 79, Amer. Geophys. Union, 105–114, https://doi.org/10.1029/GM079p0105.

Diedrichsen, M. R., M. D. Flournoy, and E. N. Rasmussen, 2020: Investigating windsond observations in supercells. *Severe Local Storms Symp.: Poster Session 1*, Boston, MA, Amer. Meteor. Soc., 940, https://ams.confex.com/ams/2020Annual/meetingapp.cgi/Paper/366187.

DiGangi, E. A., D. R. MacGorman, C. L. Ziegler, D. Betten, M. Biggerstaff, and C. K. Potvin, 2016: An overview of the 29 May 2012 Kingfisher supercell during DC3. *J. Geophys. Res. Atmos.*, **121**, 14 316–14 343, https://doi.org/10.1002/2016JD025690.

Finley, C. A., M. Elmore, L. Orf, and B. D. Lee, 2023: Impact of the streamwise vorticity current on low-level mesocyclone development in a simulated supercell. *Geophys. Res. Lett.*, **50**, e2022GL100005, https://doi.org/10.1029/2022GL100005.

Fischer, J., and J. M. L. Dahl, 2022: Transition of near-ground vorticity dynamics during tornadogenesis. *J. Atmos. Sci.*, **79**, 467–483, https://doi.org/10.1175/JAS-D-21-0181.1.

Foote, G. B., and H. W. Frank, 1983: Case study of a hailstorm in Colorado. Part III: Airflow from triple-Doppler measurements. *J. Atmos. Sci.*, **40**, 686–707, https://doi.org/10.1175/1520-0469(1983)040<0686:CSOAHI>2.0.CO;2.

Garrett, R. A., and V. D. Rockney, 1962: Tornadoes in northeastern Kansas, May 19, 1960. *Mon. Wea. Rev.*, **90**, 231–240, https://doi.org/10.1175/1520-0493(1962)090<0231:TINKM>2.0.CO;2.

Grzych, M. L., B. D. Lee, and C. A. Finley, 2007: Thermodynamic analysis of supercell rear-flank downdrafts from project ANSWERS. *Mon. Wea. Rev.*, **135**, 240–246, https://doi.org/10.1175/MWR3288.1.

Haltiner, G. J., 1971: *Numerical Weather Prediction*. John Wiley and Sons, 317 pp.

——, and R. T. Williams, 1980: *Numerical Prediction and Dynamic Meteorology*. John Wiley and Sons, 496 pp.

Helmus, J. J., and S. M. Collis, 2016: The Python ARM Radar Toolkit (Py-ART), a library for working with weather radar data in the Python programming language. *J. Open Res. Software*, **4**, e25, https://doi.org/10.5334/jors.119.

Hirth, B. D., J. L. Schroeder, and C. C. Weiss, 2008: Surface analysis of the rear-flank downdraft outflow in two tornadic supercells. *Mon. Wea. Rev.*, **136**, 2344–2363, https://doi.org/10.1175/2007MWR2285.1.

Hosek, M. J., 2022: Radar and thermodynamic analysis of the 6 April 2018 Monroe, LA, tornadic supercell. M.S. thesis, School of Meteorology, University of Oklahoma, 175 pp., https://shareok.org/handle/11244/335561.

Kessinger, C. J., P. S. Ray, and C. E. Hane, 1987: The Oklahoma squall line of 19 May 1977. Part I: A multiple Doppler analysis of convective and stratiform structure. *J. Atmos. Sci.*, **44**, 2840–2865, https://doi.org/10.1175/1520-0469(1987)044<2840:TOSLOM>2.0.CO;2.

Klemp, J. B., and R. Rotunno, 1983: A study of the tornadic region within a supercell thunderstorm. *J. Atmos. Sci.*, **40**, 359–377, https://doi.org/10.1175/1520-0469(1983)040<0359:ASOTTR>2.0.CO;2.

Knupp, K. R., 1996: Structure and evolution of a long-lived, microburst-producing storm. *Mon. Wea. Rev.*, **124**, 2785–2806, https://doi.org/10.1175/1520-0493(1996)124<2785:SAEOAL>2.0.CO;2.

——, and Coauthors, 2014: Meteorological overview of the devastating 27 April 2011 tornado outbreak. *Bull. Amer. Meteor. Soc.*, **95**, 1041–1062, https://doi.org/10.1175/BAMS-D-11-00229.1.

Koch, S. E., M. desJardins, and P. J. Kocin, 1983: An interactive Barnes objective map analysis scheme for use with satellite and conventional data. *J. Climate Appl. Meteor.*, **22**, 1487–1503, https://doi.org/10.1175/1520-0450(1983)022<1487:AIBOMA>2.0.CO;2.

Kosiba, K., J. Wurman, Y. Richardson, P. Markowski, P. Robinson, and J. Marquis, 2013: Genesis of the Goshen County, Wyoming, tornado on 5 June 2009 during VORTEX2. *Mon. Wea. Rev.*, **141**, 1157–1181, https://doi.org/10.1175/MWR-D-12-00056.1.

Lee, B. D., C. A. Finley, and C. D. Karstens, 2012: The Bowdle, South Dakota, cyclic tornadic supercell of 22 May 2010: Surface analysis of rear-flank downdraft evolution and multiple internal surges. *Mon. Wea. Rev.*, **140**, 3419–3441, https://doi.org/10.1175/MWR-D-11-00351.1.

Lilly, D. K., 1986: The structure, energetics and propagation of rotating convective storms. Part II: Helicity and storm stabilization. *J. Atmos. Sci.*, **43**, 126–140, https://doi.org/10.1175/1520-0469(1986)043<0126:TSEAPO>2.0.CO;2.

Lin, G., Z. Wang, C. Ziegler, X.-M. Hu, M. Xue, B. Geerts, and Y. Chu, 2023: A comparison of convective storm inflow moisture variability between the Great Plains and the southeastern United States using multi-platform field campaign observations. *J. Atmos. Oceanic Technol.*, **40**, 539–556, https://doi.org/10.1175/JTECH-D-22-0037.1.

Liu, B., Z. Wang, Y. Cai, P. Wechsler, W. Kuestner, M. Burkhart, and W. Welch, 2014: Compact airborne Raman lidar for profiling aerosol, water vapor and clouds. *Opt. Express*, **22**, 20 613–20 621, https://doi.org/10.1364/OE.22.020613.

Majcen, M., P. Markowski, Y. Richardson, D. Dowell, and J. Wurman, 2008: Multipass objective analysis of Doppler radar data. *J. Atmos. Oceanic Technol.*, **25**, 1845–1858, https://doi.org/10.1175/2008JTECHA1089.1.

Markowski, P. M., and Y. P. Richardson, 2010: *Mesoscale Meteorology in Midlatitudes*. Wiley-Blackwell, 407 pp.

——, J. M. Straka, and E. N. Rasmussen, 2002: Direct surface thermodynamic observations within the rear-flank downdrafts of nontornadic and tornadic supercells. *Mon. Wea. Rev.*, **130**, 1692–1721, https://doi.org/10.1175/1520-0493(2002)130<1692:DSTOWT>2.0.CO;2.

——, and Coauthors, 2012a: The pretornadic phase of the Goshen County, Wyoming, supercell of 5 June 2009 intercepted by VORTEX2. Part I: Evolution of kinematic and surface

thermodynamic fields. *Mon. Wea. Rev.*, **140**, 2887–2915, https://doi.org/10.1175/MWR-D-11-00336.1.

——, and Coauthors, 2012b: The pretornadic phase of the Goshen County, Wyoming, supercell of 5 June 2009 intercepted by VORTEX2. Part II: Intensification of low-level rotation. *Mon. Wea. Rev.*, **140**, 2916–2938, https://doi.org/10.1175/MWR-D-11-00337.1.

——, Y. P. Richardson, S. J. Richardson, and A. Petersson, 2018: Aboveground thermodynamic observations in convective storms from balloonborne probes acting as pseudo-Lagrangian drifters. *Bull. Amer. Meteor. Soc.*, **99**, 711–724, https://doi.org/10.1175/BAMS-D-17-0204.1.

Marquis, J., Y. P. Richardson, P. Markowski, D. Dowell, and J. Wurman, 2012: Tornado maintenance investigated with high-resolution dual-Doppler and EnKF analysis. *Mon. Wea. Rev.*, **140**, 3–27, https://doi.org/10.1175/MWR-D-11-00025.1.

——, ——, ——, J. Wurman, K. Kosiba, and P. Robinson, 2016: An investigation of the Goshen County, Wyoming, tornadic supercell of 5 June 2009 using EnKF assimilation of mobile mesonet and radar observations collected during VORTEX2. Part II: Mesocyclone-scale processes affecting tornado formation, maintenance, and decay. *Mon. Wea. Rev.*, **144**, 3441–3463, https://doi.org/10.1175/MWR-D-15-0411.1.

Mashiko, W., 2016: A numerical study of the 6 May 2012 Tsukuba City supercell tornado. Part I: Vorticity sources of low-level and midlevel mesocyclones. *Mon. Wea. Rev.*, **144**, 1069–1092, https://doi.org/10.1175/MWR-D-15-0123.1.

Miller, R. L., 2018: Kinematics, thermodynamics, and microphysics of the 25–26 June 2015 Kansas MCS during PECAN. M.S. thesis, School of Meteorology, University of Oklahoma, 154 pp., https://shareok.org/handle/11244/299940.

——, C. L. Ziegler, and M. I. Biggerstaff, 2020: Seven-Doppler radar and in situ analysis of the 25–26 June 2015 Kansas MCS during PECAN. *Mon. Wea. Rev.*, **148**, 211–240, https://doi.org/10.1175/MWR-D-19-0151.1.

Murdzek, S. S., P. M. Markowski, and Y. P. Richardson, 2020: Simultaneous dual-Doppler and mobile mesonet observations of streamwise vorticity currents in three supercells. *Mon. Wea. Rev.*, **148**, 4859–4874, https://doi.org/10.1175/MWR-D-20-0239.1.

Murphy, T., 2018a: KULM radar data, version 1.0. UCAR/NCAR–Earth Observing Laboratory, accessed 1 November 2022, https://doi.org/10.5065/D6PV6J6B.

——, 2018b: ULM mobile radiosonde data, version 1.1. UCAR/NCAR–Earth Observing Laboratory, accessed 1 November 2022, https://doi.org/10.5065/D6Z31XGG.

——, and K. R. Knupp, 2013: An analysis of cold season supercell storms using the synthetic dual-Doppler technique. *Mon. Wea. Rev.*, **141**, 602–624, https://doi.org/10.1175/MWR-D-12-00035.1.

——, C. Palmer, C. Entremont, and J. D. Lamb, 2019: Early operational successes of the University of Louisiana Monroe's polarimetric S-band Doppler radar. *J. Oper. Meteor.*, **7**, 105–116, https://doi.org/10.15191/nwajom.2019.0708.

O'Brien, J. J., 1970: Alternative solutions to the classical vertical velocity problem. *J. Appl. Meteor.*, **9**, 197–203, https://doi.org/10.1175/1520-0450(1970)009<0197:ASTTCV>2.0.CO;2.

Orf, L., R. Wilhelmson, B. Lee, C. Finley, and A. Houston, 2017: Evolution of a long-track violent tornado within a simulated supercell. *Bull. Amer. Meteor. Soc.*, **98**, 45–68, https://doi.org/10.1175/BAMS-D-15-00073.1.

Parker, M. D., and J. M. L. Dahl, 2015: Production of near-surface vertical vorticity by idealized downdrafts. *Mon. Wea. Rev.*, **143**, 2795–2816, https://doi.org/10.1175/MWR-D-14-00310.1.

Pauley, P. M., and X. Wu, 1990: The theoretical, discrete, and actual response of the Barnes objective analysis scheme for one- and two-dimensional fields. *Mon. Wea. Rev.*, **118**, 1145–1164, https://doi.org/10.1175/1520-0493(1990)118<1145:TTDAAR>2.0.CO;2.

Potvin, C. K., A. Shapiro, and M. Xue, 2012: Impact of a vertical vorticity constraint in variational dual-Doppler wind analysis: Tests with real and simulated supercell data. *J. Atmos. Oceanic Technol.*, **29**, 32–49, https://doi.org/10.1175/JTECH-D-11-00019.1.

Ray, P. S., and K. L. Sangren, 1983: Multiple-Doppler radar network design. *J. Climate Appl. Meteor.*, **22**, 1444–1454, https://doi.org/10.1175/1520-0450(1983)022<1444:MDRND>2.0.CO;2.

——, K. K. Wagner, K. W. Johnson, J. J. Stephens, W. C. Bumgarner, and E. A. Mueller, 1978: Triple-Doppler observations of a convective storm. *J. Appl. Meteor.*, **17**, 1201–1212, https://doi.org/10.1175/1520-0450(1978)017<1201:TDOOAC>2.0.CO;2.

——, C. L. Ziegler, W. Bumgarner, and R. J. Serafin, 1980: Single- and multiple-Doppler radar observations of tornadic storms. *Mon. Wea. Rev.*, **108**, 1607–1625, https://doi.org/10.1175/1520-0493(1980)108<1607:SAMDRO>2.0.CO;2.

Raymond, W. H., 1988: High-order low-pass implicit tangent filters for use in finite area calculations. *Mon. Wea. Rev.*, **116**, 2132–2141, https://doi.org/10.1175/1520-0493(1988)116<2132:HOLPIT>2.0.CO;2.

Roberts, B., M. Xue, A. D. Schenkman, and D. T. Dawson II, 2016: The role of surface drag in tornadogenesis within an idealized supercell simulation. *J. Atmos. Sci.*, **73**, 3371–3395, https://doi.org/10.1175/JAS-D-15-0332.1.

——, ——, and D. T. Dawson II, 2020: The effect of surface drag on mesocyclone intensification and tornadogenesis in idealized supercell simulations. *J. Atmos. Sci.*, **77**, 1699–1721, https://doi.org/10.1175/JAS-D-19-0109.1.

Rotunno, R., 1981: On the evolution of thunderstorm rotation. *Mon. Wea. Rev.*, **109**, 577–586, https://doi.org/10.1175/1520-0493(1981)109<0577:OTEOTR>2.0.CO;2.

——, and J. Klemp, 1985: On the rotation and propagation of simulated supercell thunderstorms. *J. Atmos. Sci.*, **42**, 271–292, https://doi.org/10.1175/1520-0469(1985)042<0271:OTRAPO>2.0.CO;2.

Schenkman, A. D., M. Xue, and M. Hu, 2014: Tornadogenesis in a high-resolution simulation of the 8 May 2003 Oklahoma City supercell. *J. Atmos. Sci.*, **71**, 130–154, https://doi.org/10.1175/JAS-D-13-073.1.

Schlesinger, R. E., 1978: A three-dimensional numerical model of an isolated thunderstorm. Part I: Comparative experiments for variable ambient wind shear. *J. Atmos. Sci.*, **35**, 690–713, https://doi.org/10.1175/1520-0469(1978)035<0690:ATDNMO>2.0.CO;2.

Schueth, A., C. Weiss, and J. M. L. Dahl, 2021: Comparing observations and simulations of the streamwise vorticity current and the forward flank convergence boundary in a supercell storm. *Mon. Wea. Rev.*, **149**, 1651–1671, https://doi.org/10.1175/MWR-D-20-0251.1.

Shabbott, C. J., and P. M. Markowski, 2006: Surface in situ observations within the outflow of forward-flank downdrafts of supercell thunderstorms. *Mon. Wea. Rev.*, **134**, 1422–1441, https://doi.org/10.1175/MWR3131.1.

Sherburn, K. D., and M. D. Parker, 2019: The development of severe vortices within simulated high-shear, low-CAPE convection. *Mon. Wea. Rev.*, **147**, 2189–2216, https://doi.org/10.1175/MWR-D-18-0246.1.

——, ——, J. R. King, and G. M. Lackmann, 2016: Composite environments of severe and nonsevere high shear, low-CAPE

convective events. *Wea. Forecasting*, **31**, 1899–1927, https://doi.org/10.1175/WAF-D-16-0086.1.

Skinner, P. S., C. C. Weiss, M. M. French, H. B. Bluestein, P. M. Markowski, and Y. P. Richardson, 2014: VORTEX2 observations of a low-level mesocyclone with multiple internal rear-flank downdraft momentum surges in the 18 May 2010 Dumas, Texas, supercell. *Mon. Wea. Rev.*, **142**, 2935–2960, https://doi.org/10.1175/MWR-D-13-00240.1.

Tanamachi, R. L., L. J. Wicker, D. C. Dowell, H. B. Bluestein, D. T. Dawson II, and M. Xue, 2013: EnKF assimilation of high-resolution, mobile Doppler radar data of the 4 May 2007 Greensburg, Kansas, supercell into a numerical cloud model. *Mon. Wea. Rev.*, **141**, 625–648, https://doi.org/10.1175/MWR-D-12-00099.1.

Tao, T., and T. Tamura, 2020: Numerical study of the 6 May 2012 Tsukuba supercell tornado: Vorticity sources responsible for tornadogenesis. *Mon. Wea. Rev.*, **148**, 1205–1228, https://doi.org/10.1175/MWR-D-19-0095.1.

Wade, A. R., and M. D. Parker, 2021: Dynamics of simulated high-shear, low-CAPE supercells. *J. Atmos. Sci.*, **78**, 1389–1410, https://doi.org/10.1175/JAS-D-20-0117.1.

Wang, Z., and Coauthors, 2016: Airborne Raman lidar and its applications for atmospheric process studies. *EPJ Web Conf.*, **119**, 09002, https://doi.org/10.1051/epjconf/201611909002.

Weiss, C. C., D. C. Dowell, J. L. Schroeder, P. S. Skinner, A. E. Reinhart, P. M. Markowski, and Y. P. Richardson, 2015: A comparison of near-surface buoyancy and baroclinity across three VORTEX2 supercell intercepts. *Mon. Wea. Rev.*, **143**, 2736–2753, https://doi.org/10.1175/MWR-D-14-00307.1.

Wicker, L. J., and R. B. Wilhelmson, 1995: Simulation and analysis of tornado development and decay within a three-dimensional supercell thunderstorm. *J. Atmos. Sci.*, **52**, 2675–2703, https://doi.org/10.1175/1520-0469(1995)052<2675:SAAOTD>2.0.CO;2.

Wu, D., and Coauthors, 2016: Airborne compact rotational Raman lidar for temperature measurement. *Opt. Express*, **24**, A1210–A1223, https://doi.org/10.1364/OE.24.0A1210.

Yokota, S., H. Niino, H. Seko, M. Kunii, and H. Yamauchi, 2018: Important factors for tornadogenesis as revealed by high-resolution ensemble forecasts of the Tsukuba supercell tornado of 6 May 2012 in Japan. *Mon. Wea. Rev.*, **146**, 1109–1132, https://doi.org/10.1175/MWR-D-17-0254.1.

Ziegler, C. L., 1985: Retrieval of thermal and microphysical variables in observed convective storms. Part I: Model development and preliminary testing. *J. Atmos. Sci.*, **42**, 1487–1509, https://doi.org/10.1175/1520-0469(1985)042<1487:ROTAMV>2.0.CO;2.

——, 1988: Retrieval of thermal and microphysical variables in observed convective storms. Part II: Sensitivity of cloud processes to variation of the microphysical parameterization. *J. Atmos. Sci.*, **45**, 1072–1090, https://doi.org/10.1175/1520-0469(1988)045<1072:ROTAMV>2.0.CO;2.

——, 2013a: A diabatic Lagrangian technique for the analysis of convective storms. Part I: Description and validation via an observing system simulation experiment. *J. Atmos. Oceanic Technol.*, **30**, 2248–2265, https://doi.org/10.1175/JTECH-D-12-00194.1.

——, 2013b: A diabatic Lagrangian technique for the analysis of convective storms. Part II: Application to a radar-observed storm. *J. Atmos. Oceanic Technol.*, **30**, 2266–2280, https://doi.org/10.1175/JTECH-D-13-00036.1.

——, 2019a: NOAA P-3 radar data, version 1.0. UCAR/NCAR–Earth Observing Laboratory, accessed 1 November 2022, https://doi.org/10.26023/WP1T-TTJM-VJ00.

——, 2019b: NOAA P-3 flight level data, version 1.0. UCAR/NCAR–Earth Observing Laboratory, accessed 1 November 2022, https://doi.org/10.26023/KE00-Q146-290Y.

——, T. Lee, and R. A. Pielke Jr., 1997: Convective initiation at the dryline: A modeling study. *Mon. Wea. Rev.*, **125**, 1001–1026, https://doi.org/10.1175/1520-0493(1997)125<1001:CIATDA>2.0.CO;2.